North Atlantic Ocean Internal Decadal Variability: Role of the Mean State and Ocean-Atmosphere Coupling

Guillaume Gastineau, Juliette Mignot, Olivier Arzel, Thierry Huck

North Atlantic Ocean internal decadal variability: role of the mean state and ocean-atmosphere coupling

Guillaume Gastineau*[1], Juliette Mignot[1]

Olivier Arzel[2] and Thierry Huck[2]

[1]*LOCEAN, Sorbonne Université/CNRS/IRD/MNHN, Paris, France*

[2]*LOPS, UMR 6523 CNRS/IFREMER/IRD/UBO, Brest, France*

April 12th, 2018

**Corresponding author address*: Dr Guillaume Gastineau, Sorbonne Université, UPMC/CNRS/IRD/MNHN, LOCEAN/IPSL, 4 place Jussieu, 75005 Paris, France.

E-mail: guillaume.gastineau@upmc.fr

Abstract:

The origin of the decadal variability in the North Atlantic Ocean is investigated in a series of coupled and ocean-only numerical experiments. Two versions of the IPSL-CM5A model are considered, differing only by their atmospheric horizontal resolution (3.75°x1.87° and 2.5°x1.25°). When the ocean model is forced by the climatological surface fluxes from the low atmospheric resolution coupled model version, a 20-year variability emerges, similar to the variability found in the coupled simulation. Such decadal variability is consistent with a large-scale baroclinic instability of the mean flow in the west European basin.

Increasing the atmospheric resolution leads to a more intense Icelandic low, which intensifies the western subpolar gyre, and warms the eastern North Atlantic subpolar gyre region. The mean state changes nearly vanish the associated internal oceanic variability under the corresponding climatological surface fluxes. Increasing the atmospheric resolution also produces a slightly weaker atmospheric stochastic forcing. Both the mean state and atmospheric variability changes are consistent with the decreasing amplitude of the variability in the coupled model.

For both model versions, the amplitude of the internal oceanic variability is strongly enhanced in the presence of atmospheric stochastic forcing. Air-sea coupling on the other hand has a moderate influence on the amplitude of the variability only in the low resolution model version, where the North Atlantic oceanic variability at 20-year increase by 23% due to coupling. The coupling effect is therefore modest and sensitive to the atmospheric horizontal resolution.

1. Introduction

The Atlantic Meridional Overturning Circulation (AMOC) is a major component of the climate system, as it transports tremendous amounts of heat northward. It has a major influence on the climate of the continents surrounding the Atlantic Ocean, as shown by models (Stouffer et al., 2006; Swingedouw et al. 2009; Velliga and Wood, 2002; Jackson et al. 2015) and paleoclimate studies (Rahmstorf, 2002 ; Clark et al., 2002). A deeper understanding of the AMOC variability also has important socio-economics benefit, as the AMOC might be predictable at decadal timescales (Keenlyside et al., 2008).

The AMOC is difficult to observe and a continuous monitoring only exists from 2005 onward (McCarthy et al., 2012; Smeed et al., 2014; Mercier et al., 2015), so that models have been extensively used to understand its decadal variability. In global climate models, the AMOC shows an important natural variability with decadal to centennial timescales in control runs using constant forcings for the greenhouse gases, aerosols or ozone. The AMOC variability might explain why the subpolar North Atlantic is the region where predictability at lead time of 2-yr to 5-yr is the largest compared to other basins in models (Meehl et al., 2014; Mignot et al., 2016). Some models show no preferred timescale (Kwon and Frankignoul, 2012), while others show two dominant time scales for the AMOC decadal variability (Frankcombe et al., 2010). The interplay between the AMOC and the freshwater balance of the Arctic Ocean has been suggested to be at the origin of a 50-70 yr timescale in models (Jungclaus et al., 2005; Frankcombe and Dijkstra, 2011). Such variability dominates for the SST during the instrumental period (Knight et al., 2006). A shorter 20-30 yr variability is also apparent at subpolar latitudes of the North Atlantic Ocean in observations (Plaut et al., 1995; Frankcombe and Dijkstra, 2009; Chylek et al. 2011) and many models (Menary et al., 2015). Several idealized studies of the North Atlantic basin have suggested that the 20-30 yr timescale

67 is fixed by the transit time of unstable planetary waves propagating westwards (Colin de
68 Verdière and Huck, 1999; te Raa and Dijkstra, 2002; Sévellec and Fedorov, 2010). The
69 present study focuses on the IPSL (Institut Pierre Simon Laplace) models (IPSL-CM5A-
70 LR which uses a relatively low atmospheric horizontal resolution 3.75°x1.87° and IPSL-
71 CM5A-MR based on a slightly higher atmospheric resolution 2.5°x1.25°) that show such
72 20-yr variability (Escudier et al., 2013; Wen et al., 2016; Ortega et al., 2015; Muir and
73 Fedorov, 2017). What is the precise role of air-sea coupling and atmospheric stochastic
74 forcing in this model, but also in IPSL-CM5A-MR, remains to be determined. The intent
75 of this paper is to serve as a continuation of the previous works realized with the IPSL
76 models by addressing these central questions.

77 The processes responsible for the AMOC decadal climate variability were
78 reported to be either due to (1) the atmospheric stochastic forcing (Frankignoul and
79 Hasselman, 1977; Delworth and Greatbatch, 2000), (2) self-sustained oceanic intrinsic
80 variability (Sérazin et al., 2016; Arzel et al., 2018) or (3) coupled mode of variability
81 (Timmermann et al., 1998). Most low resolution ocean models show little variability
82 when using bulk formulation as surface boundary condition (Danabasoglu et al., 2014).
83 However, the use of salinity restoring and the uncertainties in bulk formulations might
84 have some crucial effect on the AMOC decadal variability in such simulations. On the
85 other hand, idealized models using prescribed surface fluxes can generate a decadal
86 oceanic intrinsic variability (Colin de Verdière and Huck, 1999; Jamet et al., 2016).
87 Furthermore, Delworth and Greatbatch (2000) have shown that most of the AMOC
88 variability can be produced by atmospheric stochastic forcing. The main mode of North
89 Atlantic SST multidecadal variability, referred to as AMV (Atlantic Multidecadal
90 Variability), was reported to be mainly influenced by the atmosphere (Schneider and
91 Fan, 2007; Clement et al., 2015; Cane et al., 2017). These results are nevertheless under

92 debate because the AMOC northward heat transport was also identified as a driver of
93 the AMV (Zhang et al., 2017), and in many models AMOC intensification leads to a warm
94 AMV phase with a time lag ranging from 1 to 9 years (Muir and Fedorov, 2015).
95 Therefore, the relative role of the atmospheric forcing for the AMV is not yet fully
96 understood compared to that of ocean dynamics, and this study aims at better
97 quantifying it in a coupled model.
98 Lastly, the oceanic circulation could also have an impact on the large scale
99 atmospheric modes of variability. In many models, the SST and sea ice anomalies related
100 to the AMOC or the AMV may cause a significant atmospheric response albeit weak
101 (Gastineau et al., 2012; Peings and Magnusdottir, 2014; Peings et al., 2016). For instance,
102 in IPSL-CM5A-LR, a negative and eastward shifted North Atlantic Oscillation (NAO)
103 pattern occurs as a response to the subpolar SST anomalies (Gastineau et al., 2016), and
104 the positive phase of the NAO was also found to increase the AMOC a few years later
105 (Gastineau et al., 2012), so that the coupling may have a positive feedback for the 20-yr
106 AMOC variability. In IPSL-CM5A-MR, which, differs from IPSL-CM5A-LR by the higher
107 atmospheric resolution, the AMOC was reported to have a different atmospheric
108 response (Wen et al., 2016). It was argued that the AMOC induces a simultaneous NAO
109 anomaly, acting in turn as a strong positive feedback onto the AMOC variability. The
110 Atlantic gyre circulation may also play a role for the coupling together with the AMOC
111 (Bellucci et al., 2008; Fan and Schneider, 2012; Gastineau et al., 2013). However, ocean-
112 atmosphere coupling in models was mostly investigated using statistical analyses of
113 control coupled simulation, where causes and consequences are difficult to distinguish.
114 The last objective of the present study is to unravel the role of ocean-atmosphere
115 coupling using targeted model simulations.

In the following, we use the ocean component of the IPSL model and investigate and quantify the processes giving rise to the AMOC and AMV variability. We show that the North Atlantic exhibits a 20-yr variability originating from an internal oceanic mode. The characteristics of the variability are shown to be sensitive to the atmospheric resolution. Lastly, experiments are designed to investigate the role of atmospheric stochastic forcing and ocean-atmosphere coupling on the decadal-scale variability.

The experimental protocol and the model characteristics are presented in Section 2. The internal oceanic mode of variability is identified and analysed in Section 3. The roles of atmospheric stochastic forcing and air-sea coupling are investigated in section 4. The paper concludes with a summary and a discussion.

2. Data and methods

a. Coupled Model

This study uses the outputs of the IPSL-CM5A-LR and IPSL-CM5A-MR model CMIP5 (Coupled Model Intercompariason Project, phase 5) preindustrial control simulations (Dufresne et al., 2013), referred to as COUPLED-LR and COUPLED-MR in the following. Hereafter, we focus on periods of 500-yr in COUPLED-LR and 300-yr in COUPLED-MR, consistent with the periods used in Gastineau et al. (2013) and Wen et al. (2016) respectively.

Both COUPLED-LR and COUPLED-MR use the same ocean component, i.e. the NEMOv3.2 ocean model with the ORCA2 grid (resolution of about 2°) and 31 vertical levels. These model versions use the LIM-2 sea-ice component and the PISCES oceanic biogeochemistry model. The atmospheric component is the LMDZ–A model with the ORCHIDEE land surface module. The atmospheric model has 39 vertical levels and a horizontal resolution of 3.75° x1.87° in COUPLED-LR and 2.5° x 1.25° in COUPLED-MR.

Apart from the resolution, the two atmospheric configurations have the same physics, and differ only by some of their tuning parameters.

The mean AMOC of the COUPLED simulations is weak, with a yearly mean value at 40°N of about 10 Sv in LR, and 12 Sv in MR. This weak AMOC is linked to a cold bias that is present in both model versions at mid-latitudes, with smaller amplitude in COUPLED-MR (-1.4K in LR and -0.4K in MR for the global land surface air temperature; Dufresne et al., 2013). The overextended sea ice inhibits the oceanic convection in the Labrador Sea, while it overestimates it south of Iceland (Escudier et al., 2013). Despites these deficiencies, the North Atlantic atmospheric variability in COUPLED-MR and COUPLED-LR was shown to be realistic (Cattiaux et al., 2013), with fairly realistic air-sea interactions (Gastineau et al., 2013). Both model versions show jet streams that are too far equatorward, but the improved resolution in COUPLED-MR leads to a more realistic location of the jet stream (Arakelian and Codron, 2012).

b. Ocean-only simulations

To investigate the North Atlantic variability, we perform several ocean-only experiments, using the same ocean component (NEMO) as in the coupled models, but without using the sea ice (LIM2) and biogeochemistry (PISCES) modules. We use the NEMO version 3.6, using the same parameterization and parameters as the coupled simulations (see Dufresne et al., 2013 for details). The time-varying daily surface turbulent and radiative fluxes, the surface wind stress and the freshwater fluxes (evaporation minus precipitation) are taken from the COUPLED simulations described above. The river runoff and sea-ice concentration are set to a mean climatological field, both computed from COUPLED simulations. The sea-ice concentration is prescribed with a simple representation of the heat and salt exchanges in presence of sea-ice. In case of

166 sea-ice, the SST is restored to the freezing point and a constant upward flux is added.
167 The freshwater fluxes are modified so that the change in buoyancy fluxes remains
168 negligible (Madec, 2015). Therefore, the ocean-only simulations investigated in the
169 following do not consider sea ice-ocean interactions. Such interactions are important to
170 reproduce realistic heat and salt exchanges between the North Atlantic and the Arctic,
171 which can be dominant for the Atlantic multidecadal variability in other coupled models
172 (i.e. Frankcombe and Dijkstra 2011; Jungclaus et al., 2005).

173 To avoid any spurious drift and allow some damping of the surface anomalies, we
174 use a weak surface restoring for temperature and salinity. Such temperature and salinity
175 nudging are done via a Haney restoring term, where the strength of the nudging is set by
176 the coefficient γ_S and γ_T (see Servonnat et al., 2014 for details in the restoring
177 procedure). We use a relatively weak value of 10 W m^{-2} K^{-1} for γ_T, which is smaller than
178 the typical surface heat flux feedback inferred from observations over the North Atlantic
179 (around 40 W m^{-2} K^{-1}, Frankignoul and Kestenare, 2002). The SSS restoring coefficient γ_S
180 is -50 mm day^{-1}, equivalent to a restoring timescale of 2.5 yr for a 50 m mixed layer,
181 much longer than typical values used in coordinated ocean-only simulations using bulk
182 formula (Griffies et al. 2014).

183 The experiments follow the experimental protocol of Delworth and Greatbatch
184 (2000). The first set of simulations, called CLIM, are integrated over 500-yr, using a
185 repeated cycle of daily climatological heat fluxes, wind stresses and atmospheric
186 freshwater fluxes computed from the COUPLED simulations. It is designed to quantify
187 the internal ocean dynamics. In the second set of simulations, called TOTAL, the applied
188 surface forcing consists in the daily time series of the daily surface fluxes from the
189 COUPLED simulations. The TOTAL experiment is integrated over 500 yr (300 yr) for the
190 LR (MR) case. To test the robustness of the results from TOTAL, we repeat this

191 experiment with five different start dates using initial conditions sampled every 100-yr
192 from the first TOTAL run. The last set of simulations, called RANDOM, is designed to
193 assess the impact of atmospheric stochastic forcing on the oceanic variability. The
194 RANDOM experiments use randomly selected year from the TOTAL daily surface fluxes
195 forcing. To account for time autocorrelation at interannual time scale, the selection of
196 the year uses random permutations of 3-years blocks. This procedure was repeated
197 three (six) times consecutively to derive the forcings of two simulations of 1500-yr
198 (1800-yr) for the LR (MR) case. This procedure should randomize the atmospheric
199 forcing and attenuate any potential influence of the decadal frequencies included in the
200 forcing from TOTAL. The ocean-only experiments CLIM, TOTAL and RANDOM are
201 repeated for the two model versions (LR and MR), to study the impact of atmospheric
202 resolution. Unless stated otherwise, all runs are initialized from the initial state of the
203 COUPLED runs.
204
205 *c. Statistical analysis and climate indices*
206 To better highlight the decadal variability, we apply in the following a smoothing
207 to several yearly time series. We use a low-pass Lanczos filter with a cutoff period of 10-
208 yr and 21 weights, or a band-pass Lanczos filter with 10-yr and 30-yr as cutoff period
209 and 31 weights. The amplitude of the variability is quantified with the standard
210 deviation of the raw or filtered time series, after removal of a quadratic trend. When
211 using raw yearly time series, the means and standard deviation of two simulations are
212 compared using *t*-test and *F*-test, the effective number of degrees of freedom for yearly
213 time series being determined following Bretherton et al. (1999). The level of significance
214 for correlations is established using a *t*-test, with the same method (Bretherton et al.,
215 1999) to estimate the effective number of degrees of freedom. When using low-pass or

band-pass time series, we find an e-folding time scale of about 7 years for most oceanic variables, so that the total degrees of freedom are estimated by the total number of years divided by 15 when comparing two standard deviations.

The AMOC strength is computed as the maximum between 500m and 2000m depth of the Atlantic meridional overturning streamfunction averaged in 40°N-55°N. As shown by Escudier et al. (2013), the precise choice of the region used to define the AMOC strength does not alter the results as long as the AMOC is evaluated within the subpolar gyre latitudes.

The surface signature of Atlantic Ocean variability is evaluated using the AMV time series and patterns. The AMV is defined as the Atlantic ocean SST anomaly within 75°W-0°E and 0°N-60°N, smoothed by a low-pass Lanczos lowpass filter, using 10-yr as a cutoff period. The AMV pattern is obtained by the SST regression onto the standardized AMV time series.

Lastly, we calculate the NAO index with an empirical orthogonal function analysis of the monthly sea level pressure (SLP) over the North Atlantic Ocean (100°W-40°E, 20°N-90°N). The NAO index is the standardized first principal component (PC). The NAO pattern is calculated as the SLP regression onto the NAO index. The East Atlantic Pattern (EAP) is calculated similarly, but using the second PC.

d. Differences between coupled and ocean-only simulations

The ocean-only model simulations cannot reproduce the results from the COUPLED runs, as the sea ice and biogeochemistry modules are deactivated, and as the ocean-only simulations use surface restoring conditions. We first compare the mean state and variability of the coupled and ocean-only experiments. The differences of the zonal mean Atlantic temperature and salinity between the COUPLED and CLIM runs do

241 not exceed 0.4K and 0.1 psu, irrespective of the model versions used (see Supplemental
242 Material, Fig. S1). In LR, some large temperature differences (~0.3K) are located in the
243 Arctic and Southern Ocean, presumably due to the different sea ice representation. In
244 CLIM-MR, a large negative salinity anomaly is simulated at 20°N-55°N 1000-2500m in
245 the Atlantic Ocean. For both LR and LR we also note a warm (1K) and salty (~0.2 psu)
246 bias in the ocean-only runs located in the upper 500m of the ocean at 45°N and, to a
247 lesser extent, at 30°S. The tropics have a cold bias of about 0.4 K at 15°N-15°S only
248 present in the upper 50m. The mean North Atlantic SST over the AMV region is 18.7°C
249 for CLIM-LR and 19.7°C for CLIM-MR, which is consistent with the results from the
250 COUPLED simulations (18.5°C and 19.5°C respectively). The mean state difference in
251 TOTAL-LR shows a similar pattern but with larger amplitudes with typical maximum
252 large-scale anomalies of ~0.5K and ~0.1 psu below 500m. TOTAL-MR shows again a
253 fresh anomaly at 20°N-55N more pronounced than in TOTAL-LR. The RANDOM
254 simulations are similar to TOTAL (not shown).
255 Figure 1 illustrates the yearly AMOC variability in the COUPLED and TOTAL
256 simulations. The AMOC averaged over 40°N-55°N in TOTAL-MR (9.30 Sv) is larger than
257 TOTAL-LR (8.61 Sv), as expected from the corresponding coupled simulations. The
258 amplitude of the AMOC variability is estimated by the standard deviation of the raw and
259 low-pass time series (see numbers in Fig. 1 and Table 1). As expected, the variability in
260 TOTAL and COUPLED is similar (correlation r=0.83 in LR, r=0.63 in MR), but the
261 amplitude is smaller in the ocean-only runs. The difference in mean value or standard
262 deviation is larger between the TOTAL and COUPLED for the MR simulation, with an
263 AMOC 1.5 Sv weaker in TOTAL from 2020 to 2280 and a larger spread among the five
264 ensemble members. The different behavior of the LR and MR versions is presumably
265 linked to the different mean state bias, with a more intense fresh anomaly in the

266 subpolar Atlantic in TOTAL-MR. This may be due to the impacts of the different surface
267 boundary condition used, and the missing sea ice interactions. Ocean-only runs under
268 climatological surface fluxes (CLIM, Fig. 2) also exhibit a significant but weak variability,
269 with standard deviations in the AMOC low-pass index reaching only 29.1% and 10.0% of
270 that obtained in COUPLED for the LR and MR runs respectively.

271 Figure 3a-d shows the standard deviation of the yearly upper ocean potential
272 temperature averaged between 0m and 700m depth, after removal of a quadratic drift in
273 COUPLED and TOTAL. The overall spatial pattern of the COUPLED simulations is well
274 captured in TOTAL, irrespective of the atmospheric horizontal resolution, with a weaker
275 variance in MR than in LR (note difference in color bars). The agreement in term of
276 amplitude of temperature variability between COUPLED and TOTAL is, however, much
277 better for the LR than the MR runs. In CLIM-LR, the temperature variance over the
278 subpolar Atlantic basin shows a weak maximum in the subpolar Atlantic, centered at
279 55°N (Fig. 3g). CLIM-MR (Fig. 3h) has a weaker variance, but it still displays a broad
280 maximum west of the mid-Atlantic ridge in the Newfoundland Basin and downstream. In
281 both CLIM simulations, the standard deviation is typically 20% to 30% that of the
282 TOTAL simulation. RANDOM provides results similar to TOTAL and will be discussed
283 later.

284 The SST signature of ocean variability is then illustrated using the AMV patterns
285 in Fig. 4. A horseshoe shaped pattern similar to that observed (Knight et al., 2006) with
286 maximum amplitude over the subpolar basin is obtained in COUPLED at either low or
287 medium atmospheric horizontal resolutions (Fig. 4ab). SST variations are larger at low
288 resolutions. As expected from the use of SST restoring, the amplitude of the AMV is
289 significantly reduced in ocean-only runs. However the overall pattern in TOTAL remains
290 comparable to that obtained in COUPLED (Fig. 4cd), with amplitudes of SST anomalies

about half smaller. The AMV pattern in CLIM (Fig. 4gh) is even weaker than in TOTAL, but the maximum amplitude is still found in the subpolar gyre region. The amplitude is partly recovered in the RANDOM simulations, as will be commented later.

In summary, the ocean-only simulations forced by the surface fluxes diagnosed from the coupled models capture the region of maximum SST variance at subpolar latitudes, but with a smaller amplitude than in the coupled models. In the following, we will use these ocean-only simulations to interpret the decadal variability produced in the coupled models.

3. Oceanic intrinsic decadal variability

a. Climatological forcing

We first focus on the decadal variability produced in the ocean-only CLIM simulations using climatological flux forcing. The decadal variability generated in those runs is of interest as it is self-sustained and occurs without atmospheric stochastic forcing. It is the expression of the intrinsic oceanic variability. We first analyse the variability in CLIM-LR. After a relatively short transient adjustment period of about 50-yr, the AMOC and AMV in the CLIM-LR simulation exhibit clear and regular decadal oscillations (Fig. 2). The amplitude of the oscillation increases during the first 200 years of the experiment and decreases in the last 200 years, suggesting either a damped variability on a centennial time scale, or sensitive to a small mean state drift. The frequency content of the AMOC variability is further illustrated in Fig. 5 in order to better characterize the self-sustained oceanic intrinsic variability. In CLIM-LR (Fig. 5a, red line), the AMOC variance shows a clear maximum around 15-yr to 25-yr, while a peak at 20yr is found in COUPLED-LR (Fig. 5b, black line). The AMV in CLIM-LR has a very similar variability (Fig. 2 lower panel). Its pattern (Fig. 4g) has anomalies centered

316 in the subpolar regions at 55°N with negligible tropical SST anomalies, so that the typical
317 AMV horseshoe shape is not reproduced. The amplitude is 0.3K for the maximum
318 subpolar AMV SST anomalies, so that the subpolar AMV amplitude is reduced by 30% or
319 40% when compared to the fully coupled model.
320 As the atmospheric fluxes imposed in the CLIM-LR simulation have no
321 interannual or decadal variability, the decadal variability obtained here can only be
322 ascribed to an intrinsic oceanic mode. Using a similar experimental protocol, Delworth
323 and Greatbatch (2000) analysed the variability produced by the GFDL coupled model,
324 which showed a pronounced variability for periods between 70 years and 100 yr. They
325 found that such variability was not reproduced in their oceanic run using climatological
326 flux forcing. It is likely that the oceanic mode detected here was more damped or not
327 detected in the simulation of Delworth and Greatbatch (2000). The processes leading to
328 this variability will be discussed in the following section.
329 The results based on the MR configuration are contrasting. The AMOC and AMV
330 variability is much weaker in CLIM-MR after a 50-yr adjustment period (Fig. 2, dashed
331 line). In CLIM-LM, the AMOC has enhanced power for periods of 25-yr and beyond (Fig.
332 5d, red line), but no periodicity dominates at decadal time scales, with again levels of
333 variability weaker than CLIM-LR (scale of y-axis different in Fig. 5ad and 5be). The AMV
334 (Fig. 4h) shows two bands of positive anomalies, at 45°N and 55°N in the Atlantic Ocean,
335 with a maximum amplitude of 0.1K. The ocean internal variability emerging from the
336 subpolar regions in CLIM-LR is, therefore, likely to have a much weaker influence in
337 CLIM-MR, and little internal oceanic mode is found when using the climatological forcing
338 from the COUPLED-MR runs, as found in Delworth and Greatbatch (2000). The reasons
339 for this different behavior in the MR and LR configuration will be discussed later.
340

b. Processes of intrinsic oceanic variability in CLIM-LR

To illustrate the variability of the subpolar Atlantic basin found in CLIM-LR, the time evolution of the sea water density anomalies averaged between 0m and 700m and between 50°N and 60°N in latitude (see dashed box in Fig. 3, bottom) is shown in Fig. 6a as a function of longitude. Anomalies appear around 25°W, at the east of the mid-Atlantic ridge, in the west European basin, with a periodicity of about 20-yr. They propagate from 25°W to 40°W in about 6-yr, with a speed of about 0.5 cm s^{-1}. Then, they vanish at 45°W, at the southern tip of Greenland. The AMOC (Fig. 6b) is maximum one or two years after formation of the negative density anomalies at 25°W. The subpolar north Atlantic basin is then marked by a large east-west density anomaly dipole which is associated with an anomalous northward current. The AMV maximum occurs 6-yr to 7-yr years after the maximum AMOC (Fig. 6c and Fig. 7a, red line), which is consistent with a delayed impact of the intensified northward heat transport following the AMOC intensification.

The physics of the internal oceanic variability in CLIM-LR can be understood with previous studies based on the IPSL-CM5A-LR model (Ortega et al., 2015) or on the linear and adjoint version of the same ocean model (Sévellec and Fedorov, 2013). The characteristics of the mode include a westward propagation of unstable planetary waves at subpolar latitudes, a quarter phase lag between surface and subsurface temperature anomalies in the region of growth of perturbations, and a period of about 20 years. Large-scale baroclinic instability has been shown to be at the heart of the existence of such internal oceanic modes in idealized geometry (Colin de Verdière and Huck, 1999). In CLIM-LR, the region of growth for perturbations is located around 25°W - 55°N, at the south-western edge of the deep water formation site, in the west European basin, as illustrated by the regression of the upper 700m seawater density onto the AMOC (Fig.

8a). The density anomalies are dominated by the temperature anomalies (Fig. 8d). The regression of the density when AMOC is leading by 5-yr (Fig. 8b) illustrates that negative anomalies have propagated westward, consistently with Fig. 6, while positive density anomalies dominated by the salinity appear at 50°N off Newfoundland (Fig 8e). Hence, the surface salinity anomalies in the Labrador Sea might act as a positive feedback for the oceanic variability, as they are advected by the mean surface current to the main region of deep water formation, as found in Escudier et al. (2013) or Ortega et al. (2015). The density lagging by 9-yr shows a pattern opposite to that in phase with the AMOC (Fig. 8c).

The process for the oceanic variability in CLIM-LR can be further investigated using the density variance budget, following Arzel et al. (2006), with the equation below:

$$\frac{1}{2}\frac{\partial \langle \overline{\rho'^2} \rangle}{\partial t} = -\langle \overline{\boldsymbol{u}}.\boldsymbol{\nabla}\overline{\rho'^2} \rangle - \langle \overline{\boldsymbol{u}'\rho'}.\boldsymbol{\nabla}\bar{\rho} \rangle + \langle \overline{\rho' B'} \rangle + \langle \overline{\rho' D'} \rangle \qquad (1)$$

where ρ is the sea water density. The overbar and prime denote respectively time average over the whole simulation, and deviation from the time average. The angle brackets denote depth average over the top 700 m. *B'* is the net anomalous density forcing calculated from the surface freshwater and heat flux integrated within the oceanic mixed layer, assuming a linear equation of state. D' is the density tendency due to the parameterized turbulent diffusion. $\boldsymbol{u}$ is the oceanic current. The first term on the rhs represents the advection of density variance by the mean flow. The second term is positive when eddy fluxes are oriented down the mean density gradient, and was previously associated with baroclinic instabilities (Colin de Verdière and Huck, 1999). The third term is associated with the surface boundary conditions: positive values indicate that air-sea interactions increase the density variance and contribute thereby to the development of the variability, while negative ones imply a damping of the

variability by air-sea coupling. The last term represents the dissipation of variance by convective mixing and turbulent eddy diffusion and is always negative.

The different terms of the density variance budget computed from yearly outputs are shown in Fig. 9 (shading, left panels) for CLIM-LR, together with the mean current averaged over 0-300m (vectors). Most of the growth of density variance is caused by the action of the eddy fluxes (Fig. 9c) in the west European basin, at 30°W 52°N, and in the Irminger Sea. Such density flux in the west European basin is dominated the meridional component and are mainly due to temperature-driven density anomalies (not shown), as found in Fig. 8d. The advection of the density variance (Fig. 9e) transports the variance downstream of the mean currents while surface buoyancy fluxes (Fig. 9g) are weak and act as a damping. This analysis strongly suggests that the existence of low-frequency variability in CLIM-LR is due to a (large-scale) baroclinic instability of the mean flow in the west European basin. This conclusion is supported by the vertical structure of the temperature anomalies between 100 m and 1500 m (see Supplemental Material, Fig. S2) that exhibits a phase-lag of about a quarter period, with the surface anomalies leading the deeper ones, in agreement with the organization of perturbations in a zonal shear flow under quasi-geostrophic dynamics. We did not find any major sources of density variability in the Labrador Sea, where the salinity-driven density anomalies are found in Fig. 8e.

c. Processes of intrinsic oceanic variability in CLIM-MR

A similar analysis was performed in CLIM-MR. In this configuration, the density anomalies averaged in 0-700m and 50°N-60°N are weaker and the propagation is less periodic (not shown). The AMV has a positive correlation with the AMOC in this

414 simulation, with a maximum when the AMOC leads by 5-yr (Fig. 7b), consistent with the
415 results of CLIM-LR.
416 The AMOC is also correlated with the density anomalies at 50°N 30°W in CLIM-
417 MR. The pattern is somehow similar to that shown in Fig. 8, but the values are divided by
418 five in amplitude and we did not detect any density anomalies west of 40°W (not
419 shown). The density variance budget for CLIM-MR (Fig. 9, right panels) show that an
420 important eddy flux (Fig. 9d) does generate some density variance in the west European
421 basin, especially at 52°N 30°W and at 56°N 30°W, and North of Iceland, but those
422 instabilities are small (see different scale for left and right panels in Fig. 9). The
423 dominant eddy flux terms are at the same location as CLIM-LR, which emphasizes the
424 importance of baroclinic instability at this location. The density variance is then
425 advected by the mean flow (Fig. 9f), while the surface boundary conditions damp the
426 variability (Fig. 9h).
427 In summary, CLIM-MR shows some very weak decadal variability with
428 characteristics similar to that of CLIM-LR. We will see next that the mean state
429 difference caused by the different atmospheric resolution leads to a strong damping of
430 the oceanic intrinsic mode.
431
432 *d. Role of atmospheric resolution*
433 As discussed previously, the Atlantic Ocean decadal variability of CLIM-LR is
434 much stronger than in CLIM-MR, which is consistent with the results from the
435 corresponding coupled models. This difference may be traced back to the small
436 differences in the climatological fields forcing the ocean. Indeed, the atmospheric
437 resolution in the IPSL-CM5A model has an impact on the latitudinal position of the mid-
438 latitude westerlies (Arakelian and Codron, 2012). Consequently, COUPLED-MR

simulates stronger westerly wind stress between 50°N and 60°N, as the southward bias of the eddy driven jets in COUPLED-LR is reduced in COUPLED-MR with enhanced resolution (Dufresne et al., 2013). The mean SLP in MR (Fig. 10a) also shows a stronger Icelandic low. This might be explained by the different tuning of the atmospheric radiative budget, subgrid scale orographic parametrisation or horizontal dissipation. The more intense Icelandic low in COUPLED-MR induces stronger cold air advection over the western part of the subpolar gyre, thereby leading to more intense surface cooling (Fig. 10a) and positive density anomalies over that region (Fig. 10c-d) as compared to COUPLED-LR. Consequently, the subpolar gyre is more intense in the western Atlantic, particularly around 35°W 50°N, while it contracts and weakens in the eastern Atlantic and south of Iceland (Fig. 10c-d). This warms the west European basin and increases the stratification, which may contribute to inhibit the instability growth together with the modified oceanic current. This also modifies in MR the water transport into the convection sites located South of Iceland (blue dotted contours in Fig. 10c-d), which ultimately reduces the deep water formation South of Iceland and increases it further west, in the center of the subpolar gyre (Fig. 10b). Such a link between the subpolar gyre extent and deep convection areas has been reported in several previous studies (Hakkinen and Rhines, 2004; Hatun et al., 2005; Langehaug et al., 2012). However, these studies involve the Nordic seas rather than the convection site South of Iceland as here. The lack of penetration of the oceanic circulation into the Nordic Seas is a bias of this model with both atmospheric resolutions.

4. Role of the atmospheric stochastic forcing and coupling for the AMOC variability

a. Role of atmospheric stochastic forcing

464 The surface boundary conditions used in the RANDOM simulations do include
465 some variability beyond the seasonal cycle. That was not the case for the CLIM
466 simulations using a repeated identical seasonal cycle. In this section, the results from
467 RANDOM are analysed and compared to CLIM to illustrate the role of the atmospheric
468 stochastic forcing.
469 We first evaluate the atmospheric variability imposed to the ocean in the
470 RANDOM simulations. We characterize the atmospheric variability by the leading EOFs
471 of the North Atlantic SLP (see section 2.c for details). The NAO patterns (see
472 Supplemental Material, Fig. S3) are similar for LR and MR, but the NAO has more intense
473 centers of action in LR, with an anomaly of the Acores high of 4.3 hPa (3.8 hPa) and an
474 Icelandic low anomaly of -4.7 hPa (4.2 hPa) in LR (MR). This is consistent with a larger
475 SLP variance over most of the Atlantic Ocean in LR (see Supplemental Material, Fig. S4).
476 Fig. 5c-d (green lines) shows the spectra of the NAO associated with the surface
477 boundary conditions of the RANDOM simulations. The spectra are similar to a white
478 noise spectrum in both the LR and MR cases, which illustrates that the random
479 permutations have led to generate a stochastic atmospheric forcing consistent with the
480 one of a white noise. In summary, the amplitude of the atmospheric stochastic forcing is
481 larger in LR than in MR. Moreover, no periodicity emerges in the spectrum of the forcing
482 applied in RANDOM.
483 The AMOC resulting from the variable surface boundary condition in RANDOM
484 experiences a much larger variability than in CLIM, from interannual to interdecadal
485 timescales, irrespective of the atmospheric resolution (Table 1). The variance of the 0-
486 700m North Atlantic potential temperature (Fig. 3ef) is also much larger in RANDOM
487 when compared to CLIM, with a ratio among standard deviations of about 5 in both LR
488 and MR configurations. Nevertheless, both the AMOC and North Atlantic subsurface

489 temperature variability are larger in RANDOM-LR than in RANDOM-MR, which is
490 consistent with the larger atmospheric stochastic forcing in LR. The AMV pattern in
491 RANDOM (Fig. 4ef) has the typical coma shape with SST anomalies maximum in the
492 subpolar Atlantic and weaker anomalies in the East of the subtropical Atlantic gyre. The
493 maximum AMV anomalies in RANDOM-LR (+0.4K) are located south of the Irminger
494 basin, which coincides with that obtained in CLIM-LR (+0.3K) with slightly larger
495 amplitude. The maximum anomalies for RANDOM-MR (+0.3K) are located in the center
496 of the Atlantic Ocean at 45°N, farther east of the maximum anomalies found in CLIM-MR
497 (+0.1K) with much a larger amplitude. Again, the AMV anomalies are weaker in
498 RANDOM-MR than in RANDOM-LR as the atmospheric forcing is weaker. In both LR and
499 MR, the AMV pattern of RANDOM has many of the AMV characteristics produced by
500 TOTAL, in term of amplitude or latitudinal extension. This confirms the dominant role of
501 atmospheric stochastic forcing for the AMV characteristics, through the time integration
502 of the atmospheric noise within the oceanic mixed layer (Clement et al., 2015; Cane et
503 al., 2017), or through the excitation of the internal mode described previously.
504 The lag between the AMV and the AMOC is 5-yr in RANDOM-LR and 2-yr in
505 RANDOM-MR (Fig. 7, green line), which is shorter than the lag obtained in the CLIM
506 simulations. The correlation between the AMV and the AMOC is also smaller, but it
507 remains significant at the 5% level. We can conclude that including a stochastic forcing
508 may reduce the AMO-AMOC relationship and alter the time lag between the ocean and
509 the atmosphere.
510 Lastly, we illustrate the lagged correlation between the AMOC and NAO in Fig. 11.
511 In RANDOM-LR (green curve in the top panel), the NAO is negatively correlated with the
512 AMOC at lag 0, but it also has a marginal but significant correlation when the positive
513 NAO leads the AMOC by two years. In RANDOM-MR (bottom panel), the links are similar,

but the simultaneous relationships are larger, and the NAO has also a larger lagged influence onto the AMOC than in the LR, detected from lag -1 yr to lag -11 yr. It agrees with the influence of the NAO onto the AMOC (Eden and Willebrand, 2001; Mignot and Frankignoul, 2005; Gastineau and Frankignoul, 2012): the NAO causes a fast barotropic response through Ekman currents in phase and a delayed more persistent baroclinic response. This also shows that the delayed NAO stochastic forcing has more impact in the MR configuration than in the LR one. This reflects the lower levels of internal oceanic decadal variability found in MR, and relatively more important atmospheric stochastic forcing processes for the AMOC.

b. Role of coupling: the LR case

We have shown in section 2d that TOTAL-LR simulates a decadal variability comparable to that of the COUPLED-LR simulations in terms of AMOC (Fig. 1), subsurface temperature (Fig. 3) or AMV (Fig. 4) variability, even if the use of surface restoring leads to weaker SST anomalies. Figure 5 further illustrates that the decadal variability is weaker in TOTAL-LR when compared to COUPLED-LR, however, a maximum variance between 15-yr and 20-yr is still present for TOTAL-LR.

The role of air-sea coupling is inferred by comparing the RANDOM and TOTAL simulations. The forcing used in TOTAL includes both an atmospheric stochastic forcing and the atmospheric response to the ocean as simulated in COUPLED. This forcing may therefore include some decadal variability that may in turn modify the oceanic decadal variability. Conversely, the forcing in RANDOM is built so that the decadal variability is randomized. The forcing used in RANDOM and the oceanic variability are, therefore, uncorrelated at decadal time scale. We first focus on the LR simulations. The simulation TOTAL-LR (Fig. 5b, blue line) shows a more important variance at 15-25yr, when

539 compared to RANDOM-LR (Fig. 5b, green line). The patterns of the 0-700m potential
540 temperature standard deviation (Fig. 3) or the AMV (Fig. 4) have a large degree of
541 similarity, which confirms the dominant role of atmospheric stochastic forcing, in both
542 TOTAL-LR and RANDOM-LR. The lag between the AMOC and the AMV is also similar in
543 both simulations (Fig. 7a). However, the AMV pattern shows larger anomalies at 40°N
544 east of 40°W in RANDOM, so that the decadal variability of the SST is different in the two
545 simulations. This can be explained by the weaker negative surface heat flux feedback in
546 RANDOM, as the heat flux does not always act to damp the SST anomalies in this
547 simulation.

548 We calculate the pass-band variance of the subpolar subsurface (0-700m)
549 potential temperature and AMOC, using 10-30-yr as pass-band periods (Table 1). The
550 analysis reveals that the decadal variability in both the subpolar heat content and the
551 AMOC are larger in TOTAL than in RANDOM. This difference is significant at the 5% level
552 only when using a pass-band filtered AMOC index. We conclude that air-sea coupling
553 increases the amplitude of the intrinsic decadal variability. The pass-band (10-30-yr)
554 filtered AMOC standard deviation is further investigated in Fig. 12, illustrating that the
555 amplification of the meridional overturning streamfunction variability is not restricted
556 to the subpolar region and is simulated over the whole Atlantic basin.

557 The interplay between AMOC changes and the NAO can be inferred by computing
558 the lag correlation between those two indices (Fig. 11 black-line). The analysis shows
559 that the NAO reaches a negative phase 8 to 15 years after an AMOC maximum in TOTAL-
560 LR. This relationship is consistent with the results of COUPLED-LR, and previous studies
561 (Gastineau et al., 2013; Gastineau et al. 2016): the SST associated with the AMOC causes
562 a negative NAO atmospheric response when the AMOC leads by 8 to 15 yr. As the AMOC
563 has a dominant ~20-yr periodicity, this negative NAO response that follows by 8 to 15-

yr an AMOC intensification, occurs during an AMOC minimum. Such negative NAO pattern causes a weakening of the AMOC (Eden and Willebrand, 2001; Mignot and Frankignoul, 2005; Gastineau and Frankignoul, 2012), which may reinforce the AMOC minimum. Therefore, we speculate that the negative NAO response to an intense AMOC in LR explains the intensification of the 20-yr oceanic variability.

c. Role of coupling: the MR case

We now compare TOTAL-MR and RANDOM-MR to see the effect of coupling in the case of the MR simulations. Again, the standard deviation of the 0-700m potential temperature or the AMV patterns are roughly similar, even if the amplitudes are slightly larger in RANDOM-MR than in TOTAL-MR. The lagged correlation between the AMOC and the AMV are comparable in both simulations (Fig. 7b). The AMOC of RANDOM-MR has more variance than TOTAL-MR in particular for periods larger than 15-yr (Fig. 5e). This is consistent the larger NAO variance in RANDOM-MR at these periods (see Fig. 5e). In Table 1, the variance of the yearly AMOC and subsurface subpolar temperature also show larger values in RANDOM when compared to TOTAL. However, when using the pass-band variance at 10-30 yr, we do not detect any significant changes in the AMOC variance at the 5% level. This is consistent with Fig. 12b, where the variance of the AMOC is found to increase, although this increase is not statistically significant at the 5% level.

Lastly, a negative correlation between NAO and AMOC is found in TOTAL-MR when the AMOC leads by 5 to 10-yr (see Fig. 11b). The atmospheric response is expected to act as a positive feedback for the oceanic variability, as found in the LR case. However, the periodicity of the AMOC variability in MR is different from that of LR, with more variance at periods larger than 20-yr, so that this positive feedback is not detected here.

589 In summary, the coupling leads to a weak damping of the multi-decadal AMOC
590 variability in the MR case. As the oceanic internal variability is weak in MR, it is likely
591 that the coupling does not influence it. This difference obtained probably reflects the
592 different atmospheric stochastic forcing in RANDOM-MR and TOTAL-MR, as the NAO of
593 RANDOM-MR has more power at multi-decadal frequencies (Fig. 5f).
594

595 ## 5. Discussion and conclusions

596 We have investigated the processes of the decadal variability in the coupled
597 climate models IPSL-CM5A-LR (called COUPLED-LR) and IPSL-CM5A-MR (called
598 COUPLED-MR). In COUPLED-LR, the Atlantic subpolar basin exhibits a clear intrinsic
599 decadal variability with a 20-yr period. The variability is dominant when climatological
600 forcing (repeated seasonal cycle) derived from the coupled simulation is applied to an
601 ocean-only simulation. The variability is associated with westward propagating density
602 anomalies at 55°N in the eastern subpolar basin, similar to Sévellec and Fedorov (2013).
603 The density variance budget reveals the central role of transient temperature fluxes in
604 extracting potential energy from the mean flow to grow perturbations. This suggests
605 that the decadal variability in the model is caused by a large-scale baroclinic instability
606 of the mean flow at subpolar latitudes. In addition to this mechanism, we verified that
607 the subpolar density anomalies appear to be influenced by waters originating from the
608 East Greenland Current. Ortega et al. (2015) showed with the control simulation of IPSL-
609 CM5A-LR (identical to COUPLED-LR in the present study) that the East Greenland
610 Current leads to large salinity-dominated density anomalies in the Labrador Sea
611 entrance, that are then advected by the mean current, acting as a positive feedback for
612 the North Atlantic decadal variability. Although, we did not specifically investigate this
613 process here, we detected some salinity-driven density anomalies in the Labrador Sea,

614 so that it is likely that the same process is also playing a role in the simulation
615 investigated here.
616 We found that the MR model configuration is consistently generating less decadal
617 variability in coupled and ocean-only climatologically forced conditions. In the MR
618 simulation, the AMOC is more intense with warmer mean temperature and less sea ice
619 extent. The Icelandic low is also deeper and the westerlies are stronger over the
620 subpolar gyre. This leads to different momentum and heat air-sea exchanges acting to
621 intensify the subpolar gyre west of the mid-Atlantic ridge, and to decrease it east of the
622 ridge. The North Atlantic current is more zonal and intense, bringing more warm water
623 at surface to the west European basin where the density anomalies are generated. Both
624 the stronger stratification of the seawater in the top 700m and the different oceanic
625 currents in the west European basin may explain the lower oceanic internal variability
626 in MR. A detailed stability analysis of the oceanic state would be needed to address this
627 issue and is left for future work.
628 We did specific experiments to study the effect of atmospheric stochastic forcing
629 and that of ocean-atmosphere coupling. The atmospheric stochastic forcing strongly
630 amplifies the Atlantic decadal variability irrespective of the model version. However, the
631 NAO amplitude is larger in LR than in MR, which is consistent with a larger impact of
632 atmospheric forcing for the AMV and the AMOC variability in LR. In the case of LR, we
633 evaluate that a significant part of the North Atlantic climate variability is associated with
634 a self-sustained intrinsic oceanic mode: the standard deviation of the subpolar
635 temperature in CLIM-LR is 19% that of RANDOM-LR, while that of the AMOC at 10-30yr
636 in CLIM-LR is 44% that of RANDOM-LR (see Table 1). The coupling has a modest but
637 significant impact in COUPLED-LR, as it intensifies the AMOC variability by 23% at
638 periods of 10-30yr (see RANDOM-LR and TOTAL-LR in Table 1). In MR, the AMOC

variability at 10-30yr is weaker and hardly modified by coupling. Such weak variability is consistent with the lower internal oceanic variability and the weaker atmospheric stochastic forcing. In the MR case, the randomization of the atmospheric forcing leads to slightly more variance at periods larger than 25-yr, which enhances the AMOC multi-decadal variability when using randomized atmospheric fluxes as surface boundary conditions.

In LR, the influence of air-sea coupling is consistent with a NAO response to the AMOC anomalies, acting to enhance the internal oceanic variability. Our results could appear paradoxical when compared to the study of Wen et al. (2016), where the interplay between the NAO and the AMOC was found to produce a strong positive feedback in COUPLED-MR. However, the focus in the present study is on the decadal AMOC variability, while the important simultaneous NAO-AMOC feedbacks described by Wen et al. (2016) are mainly relevant at interannual and shorter time scales.

We have also investigated specifically the AMV pattern produced by the oceanic internal variability and by the atmospheric stochastic forcing. We found that, although the atmospheric forcing is responsible for the typical AMV latitudinal extension and the characteristic coma shape (as in Clement et al., 2015), significant anomalies can be produced locally by the oceanic internal variability in the subpolar gyre. For instance, the averaged AMV-anomaly (corresponding to one standard deviation of the AMV index) at 50°W-20°W 48°N-60°N is 0.15K in CLIM-LR, while it is equal to 0.22K in RANDOM-LR, so that up to 68% of the AMV anomalies can be produced by the oceanic internal variability in the subpolar gyre, where the AMV SST anomalies are largest. Nevertheless, additional work would be needed to investigate the processes linking the atmospheric stochastic forcing and the AMV. Indeed, the AMV can be produced by the integration of the atmospheric noise within the oceanic mixed layer through thermodynamical

processes (Frankignoul and Hasselmann, 1977; Clement et al., 2015), or by the amplification of the oceanic internal variability by atmospheric noise.

The variability generated in the IPSL-CM5A models is reproduced in the ocean-only simulations using climatological sea ice concentration with a simple representation for the air-sea exchanges at the ocean-ice interface. Such oceanic variability is therefore not sensitive to the accurate representation of the sea ice processes. Nevertheless, the experimental protocol could be repeated using the sea-ice model from the COUPLED simulation, to reduce the mean state difference between the coupled and ocean-only simulation (see Fig. 1). This would allow investigating the multi-decadal variability emerging from the North Atlantic – Arctic exchanges (i.e. Frankcombe and Dijkstra 2011; Jungclaus et al., 2005).

The experimental protocol used here could be repeated using more realistic fluxes based on observations to reveal the influence of model biases onto the decadal variability (Menary et al., 2015), in particular over the subpolar gyre region. The same methodology could also be used to understand the influence of the increasing greenhouse gases concentration, which may decrease the intensity of the AMOC and lead to a subpolar gyre cooling (Drijfhout et al., 2012; Rahmstorf et al., 2015). However, the simulations we have analysed here use a low horizontal resolution ocean model and do not include mesoscale or submesoscale eddies that also generate important levels of intrinsic oceanic variability in models using higher horizontal resolution (Gregorio et al., 2015). We are currently interesting if the large scale baroclinic instability found here can occur with increasing horizontal resolution.

Lastly, these results also have interesting implications for the role of the mean state for the decadal variability. We found that relatively small changes in the mean stratification and circulation of the Atlantic subpolar gyre, as obtained when comparing

CLIM-LR with CLIM-MR, lead to different levels of North Atlantic decadal variability. It is therefore crucial to reduce the mean bias of coupled models in the subpolar region to increase the realism of the simulated Atlantic decadal variability.

Acknowledgments.

The access to the model data used in this study is listed in the Supplementary Material. This research was supported by the French CNRS/INSU/LEFE-AO project MesoVarClim (PI: O. Arzel). This work was granted access to the HPC resources of TGCC under the allocations 2016-017403, 2017-017403 and A0030107403 made by GENCI. This study benefited from the IPSL mesocenter facility which is supported by CNRS, UPMC, Labex L-IPSL, which is funded by the ANR (Grant #ANR-10-LABX-0018), and by the European FP7 IS-ENES2 project (Grant #312979).

References

Arakelian A., & Codron, F. (2012). Southern Hemisphere jet variability in the IPSL GCM at varying resolutions. *Journal of the Atmospheric Sciences*, *69*(12), 3788–3799.

Arzel, O., Huck, T., & Colin de Verdière, A. (2006). The different nature of the interdecadal variability of the thermohaline circulation under mixed and flux boundary conditions. *Journal of physical oceanography*, *36*(9), 1703-1718.

Arzel, O., T. Huck, and A. Colin de Verdière (2018). The internal generation of the Atlantic ocean interdecadal variability. *Jornal of Climate.* https://doi.org/10.1175/JCLI-D-17-0884.1

Bellucci, A., Gualdi, S., Scoccimarro, E., & Navarra, A. (2008). NAO–ocean circulation interactions in a coupled general circulation model. *Climate Dynamics*, *31*(7–8), 759–777.

Bretherton, C. S., Widmann, M., Dymnikov, V. P., Wallace, J. M., & Bladé, I. (1999). The effective number of spatial degrees of freedom of a time-varying field. *Journal of climate*, *12*(7), 1990-2009.

Cane, M. A., Clement, A. C., Murphy, L. N., & Bellomo, K. (2017). Low-Pass Filtering, Heat Flux, and Atlantic Multidecadal Variability. *Journal of Climate*, *30*(18), 7529–7553. doi :10.1175/JCLI-D-16-0810.1

Cattiaux, J., Quesada, B., Arakélian, A., Codron, F., Vautard, R., & Yiou, P. (2013). North-Atlantic dynamics and European temperature extremes in the IPSL model: sensitivity to atmospheric resolution. *Climate Dynamics*, *40*(9–10), 2293–2310.

Chylek, P., Folland, C. K., Dijkstra, H. A., Lesins, G., & Dubey, M. K. (2011). Ice-core data evidence for a prominent near 20 year time-scale of the Atlantic Multidecadal Oscillation. *Geophysical Research Letters*, *38*(13). doi :10.1029/2011GL047501

726 Clark, P. U., Pisias, N. G., Stocker, T. F., & Weaver, A. J. (2002). The role of the
727 thermohaline circulation in abrupt climate change. *Nature*, *415*(6874), 863–869.
728 doi :10.1038/415863a
729 Clement, A., Bellomo, K., Murphy, L. N., Cane, M. A., Mauritsen, T., Rädel, G., & Stevens, B.
730 (2015). The Atlantic Multidecadal Oscillation without a role for ocean circulation.
731 *Science*, *350*(6258), 320–324.
732 Colin de Verdière, A., & Huck, T. (1999). Baroclinic instability: An oceanic wavemaker for
733 interdecadal variability. *Journal of Physical Oceanography*, *29*(5), 893–910.
734 Danabasoglu, G., Yeager, S. G., Bailey, D., Behrens, E., Bentsen, M., Bi, D., … Canuto, V. M.
735 (2014). North Atlantic simulations in coordinated ocean-ice reference experiments
736 phase II (CORE-II). Part I: mean states. *Ocean Modelling*, *73*, 76–107.
737 Delworth, T. L., & Greatbatch, R. J. (2000). Multidecadal thermohaline circulation
738 variability driven by atmospheric surface flux forcing. *Journal of Climate*, *13*(9), 1481–
739 1495.
740 Drijfhout, S., van Oldenborgh, G. J., & Cimatoribus, A. (2012). Is a Decline of AMOC
741 Causing the Warming Hole above the North Atlantic in Observed and Modeled
742 Warming Patterns? *Journal of Climate*, *25*(24), 8373–8379. doi :10.1175/JCLI-D-12-
743 00490.1
744 Dufresne, J.-L., Foujols, M.-A., Denvil, S., Caubel, A., Marti, O., Aumont, O., … Benshila, R.
745 (2013). Climate change projections using the IPSL-CM5 Earth System Model: from
746 CMIP3 to CMIP5. *Climate Dynamics*, *40*(9–10), 2123–2165.
747 Eden, C., & Willebrand, J. (2001). Mechanism of interannual to decadal variability of the
748 North Atlantic circulation. *Journal of Climate*, *14*(10), 2266–2280.

749 Escudier, R., Mignot, J., & Swingedouw, D. (2013). A 20-year coupled ocean-sea ice-
750 atmosphere variability mode in the North Atlantic in an AOGCM. *Climate Dynamics*,
751 *40*(3), 619–636. doi :10.1007/s00382-012-1402-4
752 Fan, M., & Schneider, E. K. (2012). Observed decadal North Atlantic tripole SST
753 variability. Part I: weather noise forcing and coupled response. *Journal of the*
754 *Atmospheric Sciences*, *69*(1), 35–50.
755 Frankcombe, L. M., & Dijkstra, H. A. (2009). Coherent multidecadal variability in North
756 Atlantic sea level. *Geophysical Research Letters*, *36*(15).
757 Frankcombe, L. M., & Dijkstra, H. A. (2011). The role of Atlantic-Arctic exchange in North
758 Atlantic multidecadal climate variability. *Geophysical Research Letters*, *38*(16), n/a-
759 n/a. doi :10.1029/2011GL048158
760 Frankcombe, L. M., Von Der Heydt, A., & Dijkstra, H. A. (2010). North Atlantic
761 multidecadal climate variability: an investigation of dominant time scales and
762 processes. *Journal of Climate*, *23*(13), 3626–3638.
763 Frankignoul, C., & Hasselmann, K. (1977). Stochastic climate models, Part II Application
764 to sea-surface temperature anomalies and thermocline variability. *Tellus*, *29*(4), 289–
765 305.
766 Frankignoul, C., & Kestenare, E. (2002). The surface heat flux feedback. Part I: estimates
767 from observations in the Atlantic and the North Pacific. *Climate Dynamics*, *19*(8), 633–
768 647.
769 Gastineau, G., D'Andrea, F., & Frankignoul, C. (2013). Atmospheric response to the North
770 Atlantic Ocean variability on seasonal to decadal time scales. *Climate Dynamics*, *40*(9–
771 10), 2311–2330.

772 Gastineau, G., & Frankignoul, C. (2012). Cold-season atmospheric response to the natural
773 variability of the Atlantic meridional overturning circulation. *Climate Dynamics*, *39*(1–
774 2), 37–57.
775 Gastineau, G., L'hévéder, B., Codron, F., & Frankignoul, C. (2016). Mechanisms
776 determining the winter atmospheric response to the Atlantic overturning circulation.
777 *Journal of Climate*, *29*(10), 3767–3785.
778 Grégorio, S., Penduff, T., Sérazin, G., Molines, J.-M., Barnier, B., & Hirschi, J. (2015).
779 Intrinsic variability of the Atlantic meridional overturning circulation at interannual-
780 to-multidecadal time scales. *Journal of Physical Oceanography*, *45*(7), 1929–1946.
781 Griffies, S. M., Yin, J., Durack, P. J., Goddard, P., Bates, S. C., Behrens, E., … Böning, C. W.
782 (2014). An assessment of global and regional sea level for years 1993–2007 in a suite
783 of interannual CORE-II simulations. *Ocean Modelling*, *78*, 35–89.
784 Häkkinen, S., & Rhines, P. B. (2004). Decline of subpolar North Atlantic circulation during
785 the 1990s. *Science*, *304*(5670), 555–559.
786 Hátún, H., Sandø, A. B., Drange, H., Hansen, B., & Valdimarsson, H. (2005). Influence of the
787 Atlantic subpolar gyre on the thermohaline circulation. *Science*, *309*(5742), 1841–
788 1844.
789 Jackson, L. C., Kahana, R., Graham, T., Ringer, M. A., Woollings, T., Mecking, J. V., & Wood,
790 R. A. (2015). Global and European climate impacts of a slowdown of the AMOC in a
791 high resolution GCM. *Climate Dynamics*, *45*(11), 3299–3316. doi :10.1007/s00382-
792 015-2540-2
793 Jamet, Q., Huck, T., Arzel, O., Campin, J.-M., & Colin de Verdière, A. (2016). Oceanic
794 control of multidecadal variability in an idealized coupled GCM. *Climate Dynamics*,
795 *46*(9–10), 3079–3095.

796 Jungclaus, J. H., Haak, H., Latif, M., & Mikolajewicz, U. (2005). Arctic–North Atlantic
797 interactions and multidecadal variability of the meridional overturning circulation.
798 *Journal of Climate*, *18*(19), 4013–4031.
799 Keenlyside, N. S., Latif, M., Jungclaus, J., Kornblueh, L., & Roeckner, E. (2008). Advancing
800 decadal-scale climate prediction in the North Atlantic sector. *Nature*, *453*(7191), 84–
801 88. doi:10.1038/nature06921
802 Knight, J. R., Folland, C. K., & Scaife, A. A. (2006). Climate impacts of the Atlantic
803 multidecadal oscillation. *Geophysical Research Letters*, *33*(17).
804 Kwon, Y. O., & Frankignoul, C. (2012). Stochastically-driven multidecadal variability of
805 the Atlantic meridional overturning circulation in CCSM3. *Climate dynamics*, *38*(5-6),
806 859-876.
807 Langehaug, H. R., Medhaug, I., Eldevik, T., & Otterå, O. H. (2012). Arctic/Atlantic
808 exchanges via the subpolar gyre. *Journal of Climate*, *25*(7), 2421–2439.
809 Madec, G. (2015). NEMO ocean engine. *Note Du Pôle de Modélisation, Institut Pierre*
810 *Simon Laplace, France, Technical Report*, *27*.
811 McCarthy, G., Frajka-Williams, E., Johns, W. E., Baringer, M. O., Meinen, C. S., Bryden, H. L.,
812 … Cunningham, S. A. (2012). Observed interannual variability of the Atlantic
813 meridional overturning circulation at 26.5°N. *Geophysical Research Letters*, *39*(19).
814 doi :10.1029/2012GL052933
815 Meehl, G. A., Goddard, L., Boer, G., Burgman, R., Branstator, G., Cassou, C., … Hawkins, E.
816 (2014). Decadal climate prediction: an update from the trenches. *Bulletin of the*
817 *American Meteorological Society*, *95*(2), 243–267.
818 Menary, M. B., Hodson, D. L., Robson, J. I., Sutton, R. T., Wood, R. A., & Hunt, J. A. (2015).
819 Exploring the impact of CMIP5 model biases on the simulation of North Atlantic
820 decadal variability. *Geophysical Research Letters*, *42*(14), 5926–5934.

821 Mercier, H., Lherminier, P., Sarafanov, A., Gaillard, F., Daniault, N., Desbruyères, D., ... &
822 Thierry, V. (2015). Variability of the meridional overturning circulation at the
823 Greenland–Portugal OVIDE section from 1993 to 2010. *Progress in Oceanography*,
824 *132*, 250-261.
825 Mignot, J., & Frankignoul, C. (2005). The variability of the Atlantic meridional
826 overturning circulation, the North Atlantic oscillation, and the El Niño–Southern
827 oscillation in the Bergen climate model. *Journal of climate*, *18*(13), 2361-2375.
828 Mignot, J., García-Serrano, J., Swingedouw, D., Germe, A., Nguyen, S., Ortega, P., … Ray, S.
829 (2016). Decadal prediction skill in the ocean with surface nudging in the IPSL-CM5A-
830 LR climate model. *Climate Dynamics*, *47*(3–4), 1225–1246.
831 Muir, L., & Fedorov, A. (2015). How the AMOC affects ocean temperatures on decadal to
832 centennial timescales: the North Atlantic versus an interhemispheric seesaw. *Climate*
833 *Dynamics*, *45*(1–2), 151–160.
834 Muir, L. C., & Fedorov, A. V. (2017). Evidence of the AMOC interdecadal mode related to
835 westward propagation of temperature anomalies in CMIP5 models. *Climate Dynamics*,
836 *48*(5-6), 1517-1535.
837 Ortega, P., Mignot, J., Swingedouw, D., Sévellec, F., & Guilyardi, E. (2015). Reconciling two
838 alternative mechanisms behind bi-decadal variability in the North Atlantic. *Progress*
839 *in Oceanography*, *137*, 237–249.
840 Peings, Y., & Magnusdottir, G. (2014). Forcing of the wintertime atmospheric circulation
841 by the multidecadal fluctuations of the North Atlantic ocean. *Environmental Research*
842 *Letters*, *9*(3), 034018.
843 Peings, Y., Simpkins, G., & Magnusdottir, G. (2016). Multidecadal fluctuations of the
844 North Atlantic Ocean and feedback on the winter climate in CMIP5 control

simulations. *Journal of Geophysical Research: Atmospheres*, *121*(6), 2571–2592. Doi :10.1002/2015JD024107

Plaut, G., Ghil, M., & Vautard, R. (1995). Interannual and interdecadal variability in 335 years of central England temperatures. *Science- New York then Washington-*, 710–710.

Rahmstorf, S. (2002). Ocean circulation and climate during the past 120,000 years. *Nature*, *419*(6903), 207–214. https://doi.org/10.1038/nature01090

Rahmstorf, S., Box, J. E., Feulner, G., Mann, M. E., Robinson, A., Rutherford, S., & Schaffernicht, E. J. (2015). Exceptional twentieth-century slowdown in Atlantic Ocean overturning circulation. *Nature Clim. Change*, *5*(5), 475–480.

Schneider, E. K., & Fan, M. (2007). Weather noise forcing of surface climate variability. *Journal of the Atmospheric Sciences*, *64*(9), 3265–3280.

Sérazin, G., B. Meyssignac, T. Penduff, L. Terray, B. Barnier, and J.-M. Molines (2016), Quantifying uncertainties on regional sea level change induced by multidecadal intrinsic oceanic variability, *Geophys. Res. Lett.*, 43, 8151–8159, doi: 10.1002/2016GL069273.

Servonnat, J., Mignot, J., Guilyardi, E., Swingedouw, D., Séférian, R., & Labetoulle, S. (2015). Reconstructing the subsurface ocean decadal variability using surface nudging in a perfect model framework. *Climate Dynamics*, *44*(1–2), 315–338.

Sévellec, F., & Fedorov, A. V. (2010). Excitation of SST anomalies in the eastern equatorial Pacific by oceanic optimal perturbations. *Journal of Marine Research*, *68*(3–1), 597–624.

Sévellec, F., & Fedorov, A. V. (2013). The leading, interdecadal eigenmode of the Atlantic meridional overturning circulation in a realistic ocean model. *Journal of Climate*, *26*(7), 2160–2183.

869 Smeed, D. A., McCarthy, G. D., Cunningham, S. A., Frajka-Williams, E., Rayner, D., Johns, W.
870 E., … Duchez, A. (2014). Observed decline of the Atlantic meridional overturning
871 circulation 2004-2012. *Ocean Science*, *10*(1), 29.
872 Stouffer, R. J., Yin, J., Gregory, J. M., Dixon, K. W., Spelman, M. J., Hurlin, W., … Weber, S. L.
873 (2006). Investigating the Causes of the Response of the Thermohaline Circulation to
874 Past and Future Climate Changes. *Journal of Climate*, *19*(8), 1365–1387.
875 doi :10.1175/JCLI3689.1
876 Swingedouw, D., Mignot, J., Braconnot, P., Mosquet, E., Kageyama, M., & Alkama, R.
877 (2009). Impact of Freshwater Release in the North Atlantic under Different Climate
878 Conditions in an OAGCM. *Journal of Climate*, *22*(23), 6377–6403.
879 doi :10.1175/2009JCLI3028.1
880 Te Raa, L. A., & Dijkstra, H. A. (2002). Instability of the thermohaline ocean circulation on
881 interdecadal timescales. *Journal of Physical Oceanography*, *32*(1), 138–160.
882 Timmermann, A., Latif, M., Voss, R., & Grötzner, A. (1998). Northern Hemispheric
883 interdecadal variability: A coupled air–sea mode. *Journal of Climate*, *11*(8), 1906-
884 1931.
885 Vellinga, M., & Wood, R. A. (2002). Global climatic impacts of a collapse of the Atlantic
886 thermohaline circulation. *Climatic change*, *54*(3), 251-267.
887 Wen, N., Frankignoul, C., & Gastineau, G. (2016). Active AMOC–NAO coupling in the IPSL-
888 CM5A-MR climate model. *Climate Dynamics*, *47*(7–8), 2105–2119.
889 Zhang, R. (2017). On the persistence and coherence of subpolar sea surface temperature
890 and salinity anomalies associated with the Atlantic multidecadal variability.
891 *Geophysical Research Letters*, *44*(15), 7865–7875. doi :10.1002/2017GL074342
892

Tables

TABLE 1. AMOC and North Atlantic temperature variability in the coupled and ocean-only simulations. The star indicates when the level of significance is below 5% for the Fisher *F*-test of the variances when compared to the corresponding TOTAL simulation. The temperature variability is given by the standard deviation of the yearly supolar North Atlantic (40°N-62°N; 75°W-0°E) potential temperature between 0m and 700m.

Simulation	Surface boundary conditions	Model	AMOC std. dev. (Sv)		North Atl. Temp. std. dev. (10^{-1} K)
			Yearly	10-30yr	Yearly
COUPLED	Fully-coupled	LR	1.35*	0.64	2.01
CLIM	Climatology	LR	0.32*	0.23*	0.35*
TOTAL	Raw daily fluxes	LR	1.12	0.64	1.86
RANDOM	Randomly selected daily fluxes	LR	1.04	0.52*	1.85
COUPLED	Fully-coupled	MR	1.04*	0.43	1.73*
CLIM	Climatology	MR	0.09	0.03*	0.20*
TOTAL	Raw daily fluxes	MR	0.75	0.36	1.04
RANDOM	Randomly selected daily fluxes	MR	0.88*	0.42	1.22*

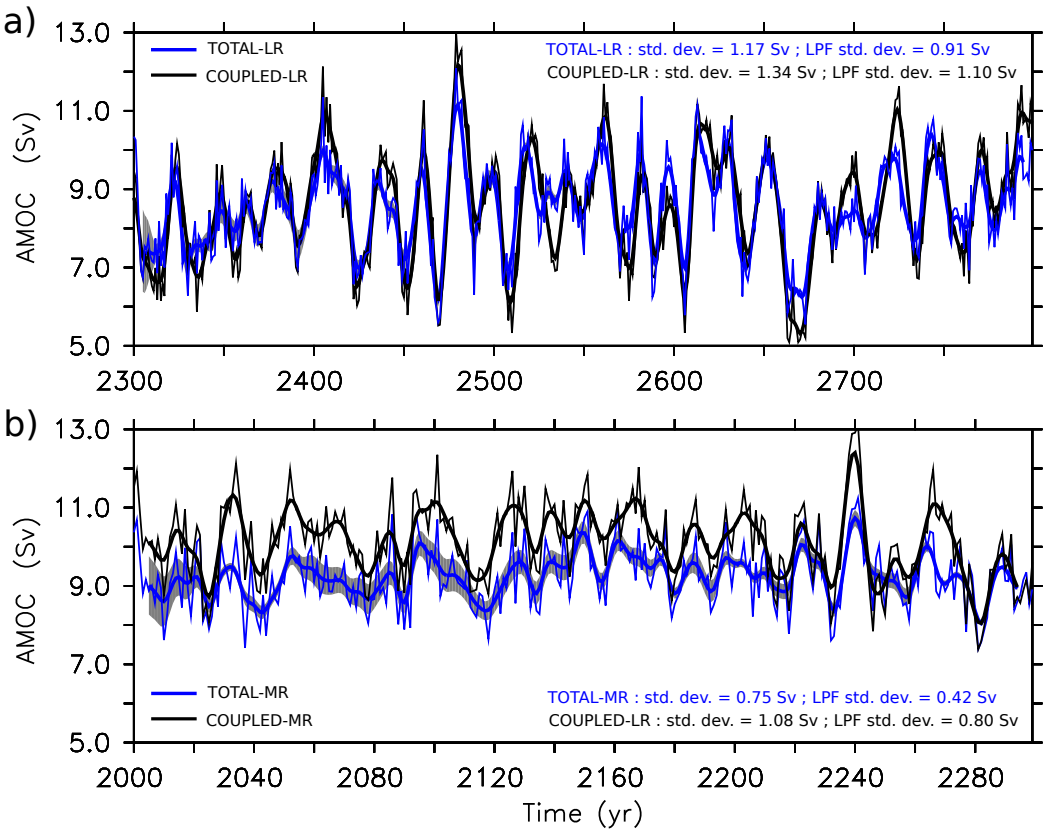

Figure 1:

AMOC time series, in Sv, for (a) the coupled simulation COUPLED-LR (black line) and the ocean-only simulation TOTAL-LR (blue line: ensemble mean; grey shades: standard deviation among members). (b) Same as (a), but for the COUPLED-MR and TOTAL-MR simulations. The standard deviation of yearly and low-pass filtered (LPF) time series is indicated in each panel.

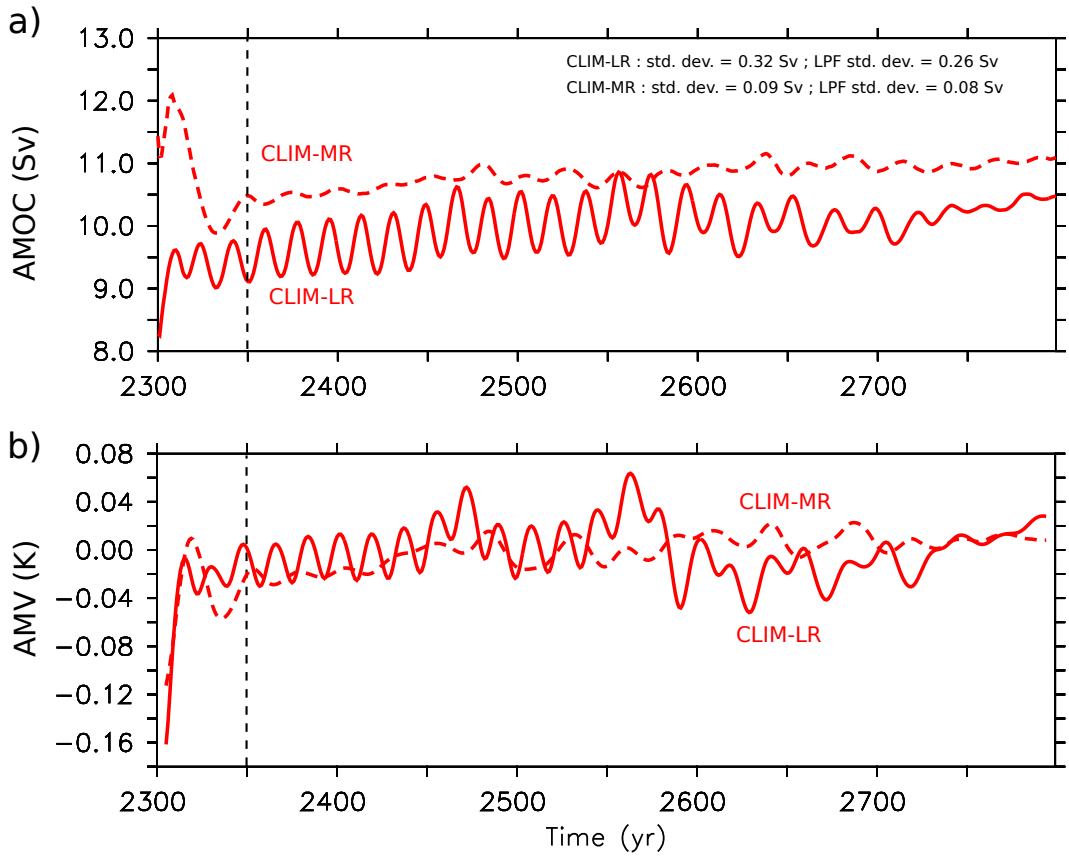

Figure 2:

(a) AMOC, in Sv, and (b) AMV, in K, yearly time series for the ocean-only simulation forced by climatological fluxes CLIM-LR and CLIM-MR. No smoothing was applied to the time series. The standard deviation of yearly and low-pass filtered (LPF) time series is indicated in (a).

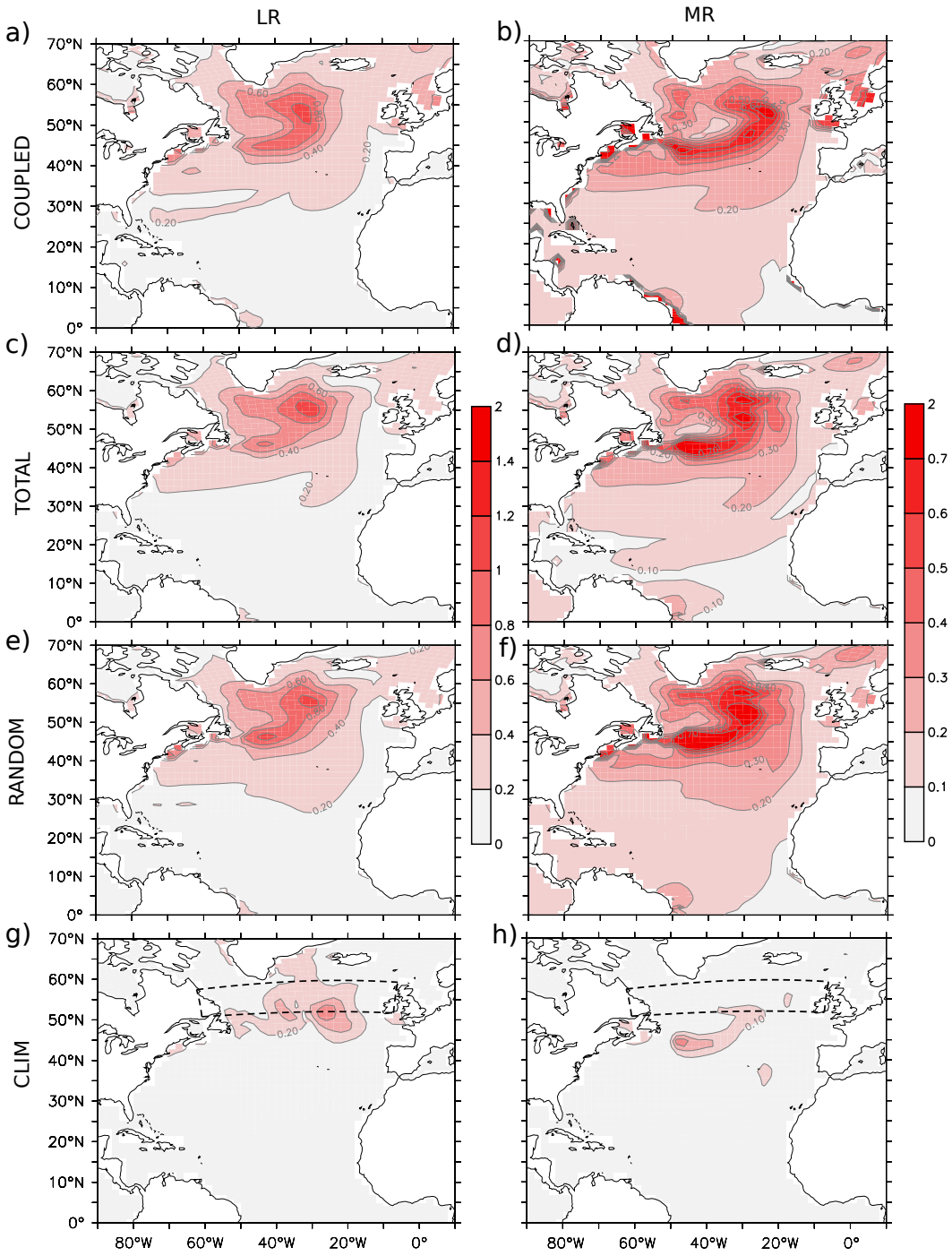

Figure 3:

Standard deviation of the yearly mean potential temperature between 0 and 700m, in K, for (a) COUPLED-LR, (b) COUPLED-MR, (c) TOTAL-LR, (d) TOTAL-MR, (e) RANDOM-LR, (f) RANDOM-MR (g) CLIM-LR and (h) CLIM-MR. Note the difference in contour intervals in the left and right panels. The black dashed lines provide the location of the latitudinal band studied in Fig. 6.

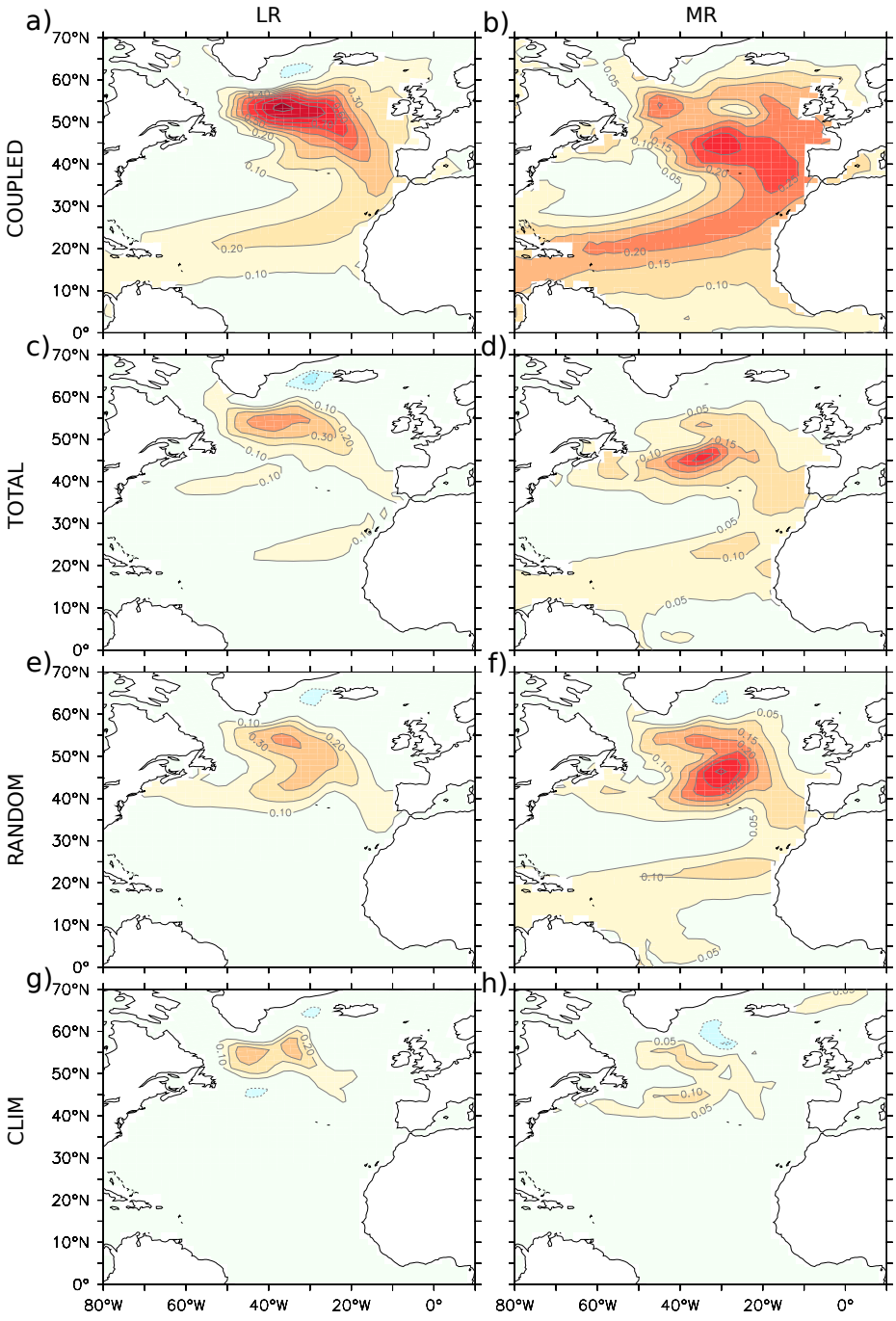

Figure 4:

AMV pattern (in K / std. dev.) in (a) COUPLED-LR, (b) COUPLED-MR, (c) TOTAL-LR, (d) TOTAL-MR, (e) RANDOM-LR, (f) RANDOM-MR, (g) CLIM-LR and (h) CLIM-MR. The contour interval is different is left and right panels.

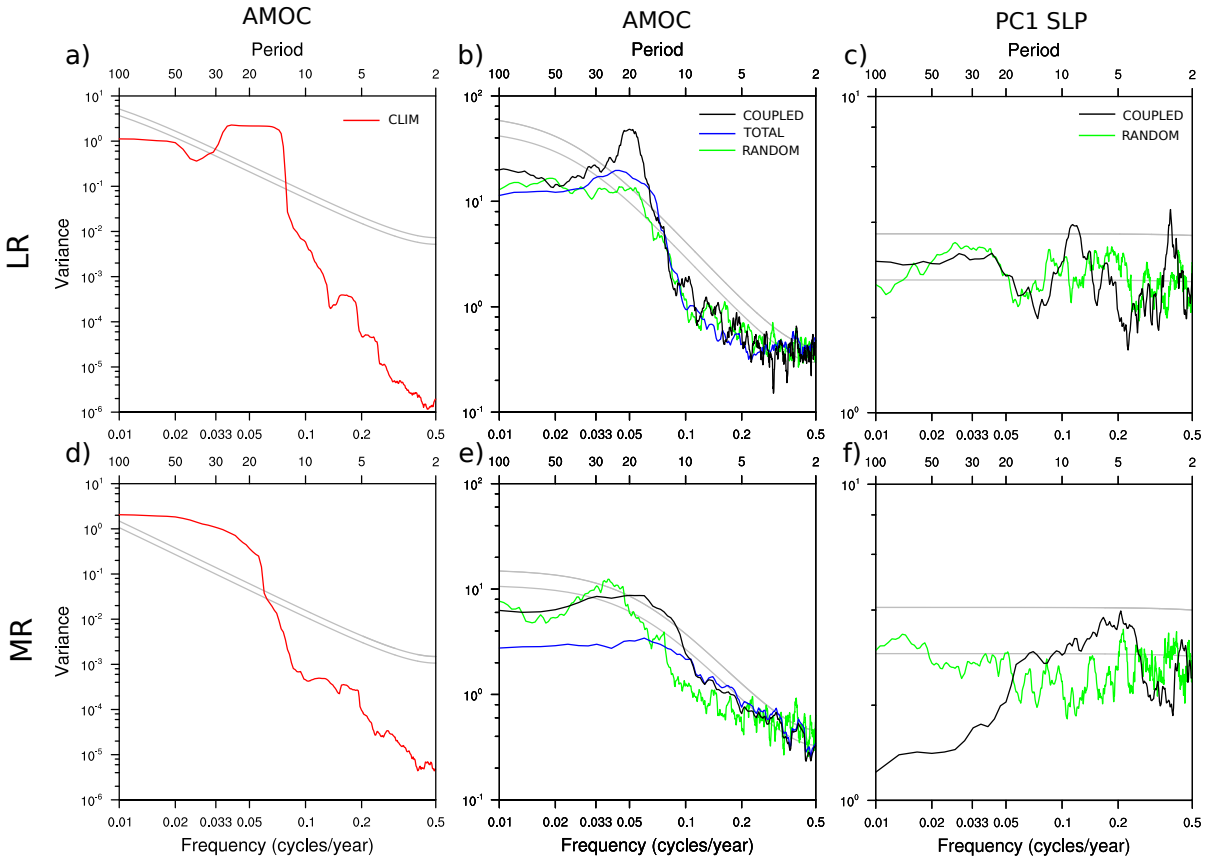

Figure 5:

(a) Variance frequency spectrum of the AMOC index for CLIM-LR. (b) Same as (a) for (green) RANDOM-LR, (blue) ensemble mean of TOTAL-LR, and (black) COUPLED-LR simulation. (c) Variance frequency spectrum of the NAO index, defined as the PC1 of the SLP for (green) RANDOM-LR and (black) COUPLED-LR simulation. (d), (e) and (f) are the same as (a), (b) and (c) for the MR simulations. The spectra are calculated via fast Fourier transform. The theoretical Markov spectrum and the upper 95% confidence curve using the lag-1 autocorrelation are shown for the CLIM (panels a) and d)) or COUPLED (panles b), c), e) and f)) simulations in grey lines. Note that the scale of the y-axis is different in each column.

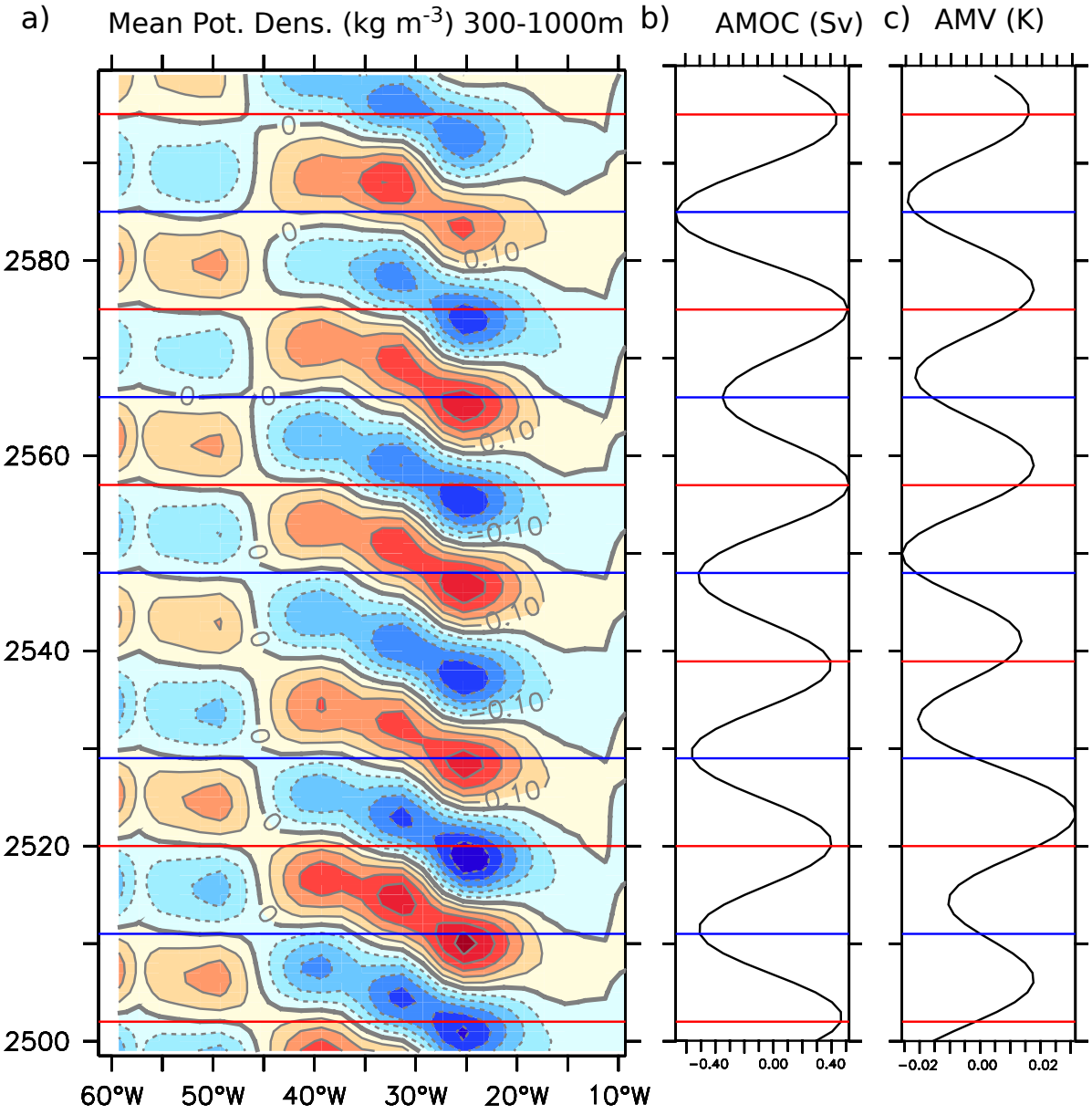

Figure 6:

(a) Seawater density anomalies (in kg m^{-3}) averaged in 50°N-60°N (region displayed in Fig. 3gh) for a period of 100-yr of CLIM-LR. (b) AMOC anomalies, in Sv, for the 100-yr period of CLIM-LR corresponding to panel (a). (c) Same as (b) but for the AMV time series, in K. The blue (red) line denotes the AMOC minimum (maximum). No smoothing was applied to the time series.

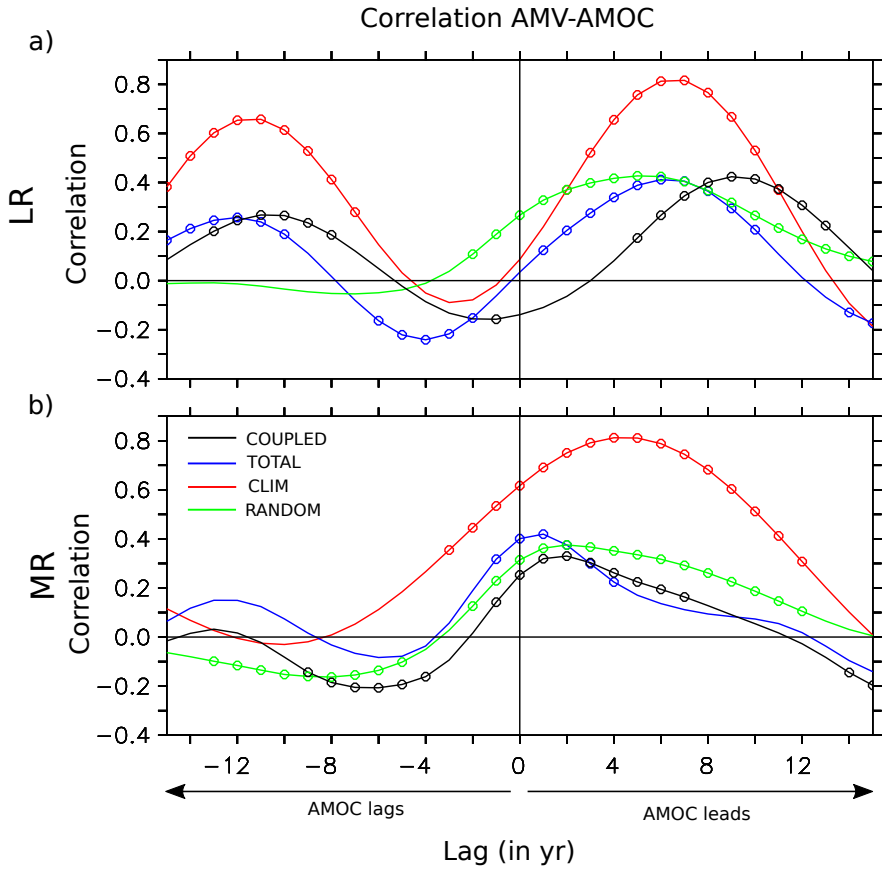

Figure 7:

Lagged correlation between the AMOC and the AMV for (a) LR and (b) MR simulations. The lag (in year) is positive when the AMOC lead. The color is black for the COUPLED simulation, red for CLIM, blue for TOTAL and green for RANDOM. The circles indicate level of significance below 5%.

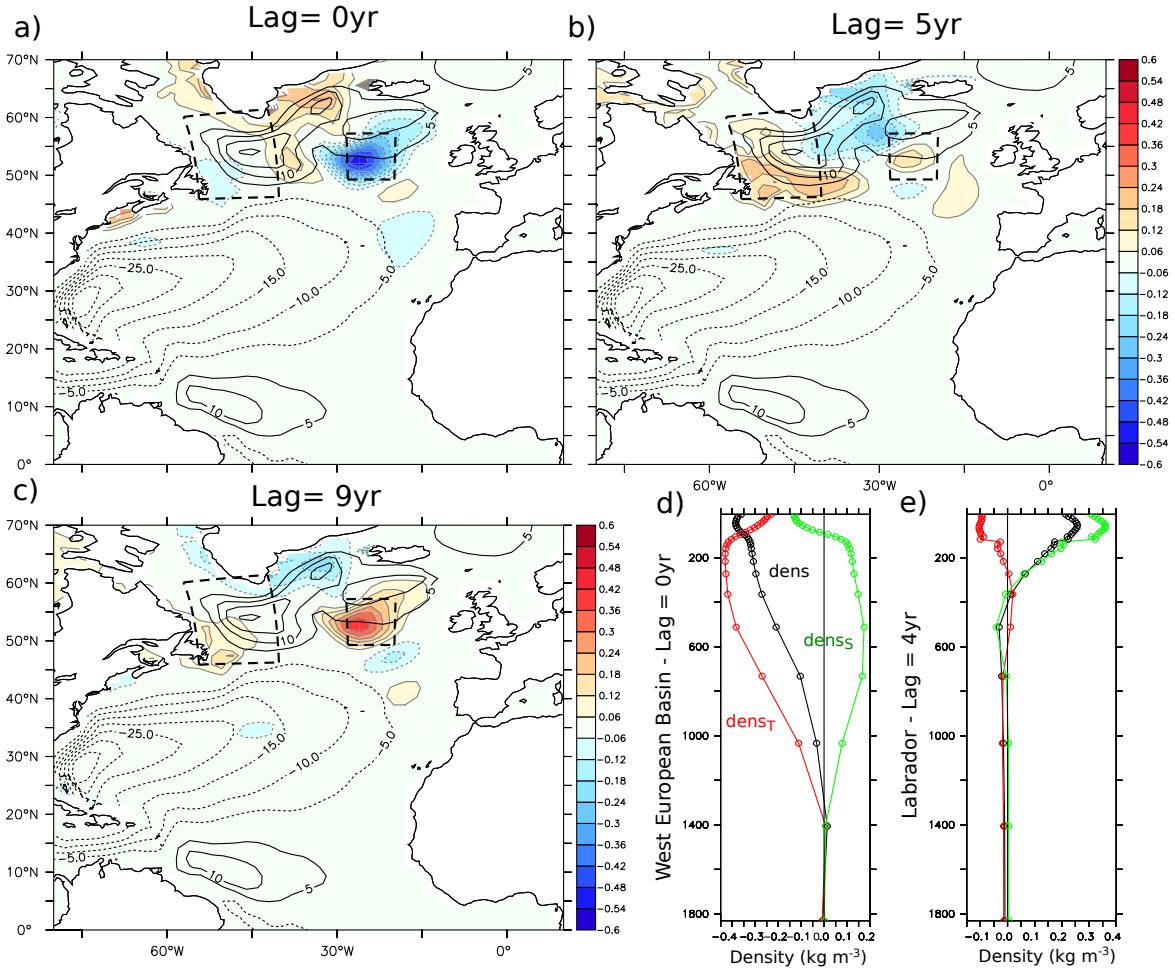

Figure 8:

Regression of the 0-700m density anomalies, (in kg m^{-3}) onto the AMOC index in CLIM-LR, for (a) simultaneous fields (Lag=0yr), (b) when the AMOC leads by 5-yr, and (c) 9–yr. The thick black contours indicate the mean barotropic streamfunction, in Sv. (d) Regression of density anomalies averaged over the west European basin with a lag of 0-yr (region illustrated by dashed lines on panels (a-c)). The black line indicate the total density anomalies, the green line indicates the salinity-driven density anomalies while the red line is the temperature-driven density anomaly. (e) Same as (d), but for the density anomalies averaged in the Labrador sea entrance with a lag of 5-yr (region illustrated by dashed lines on panels (a-c)).

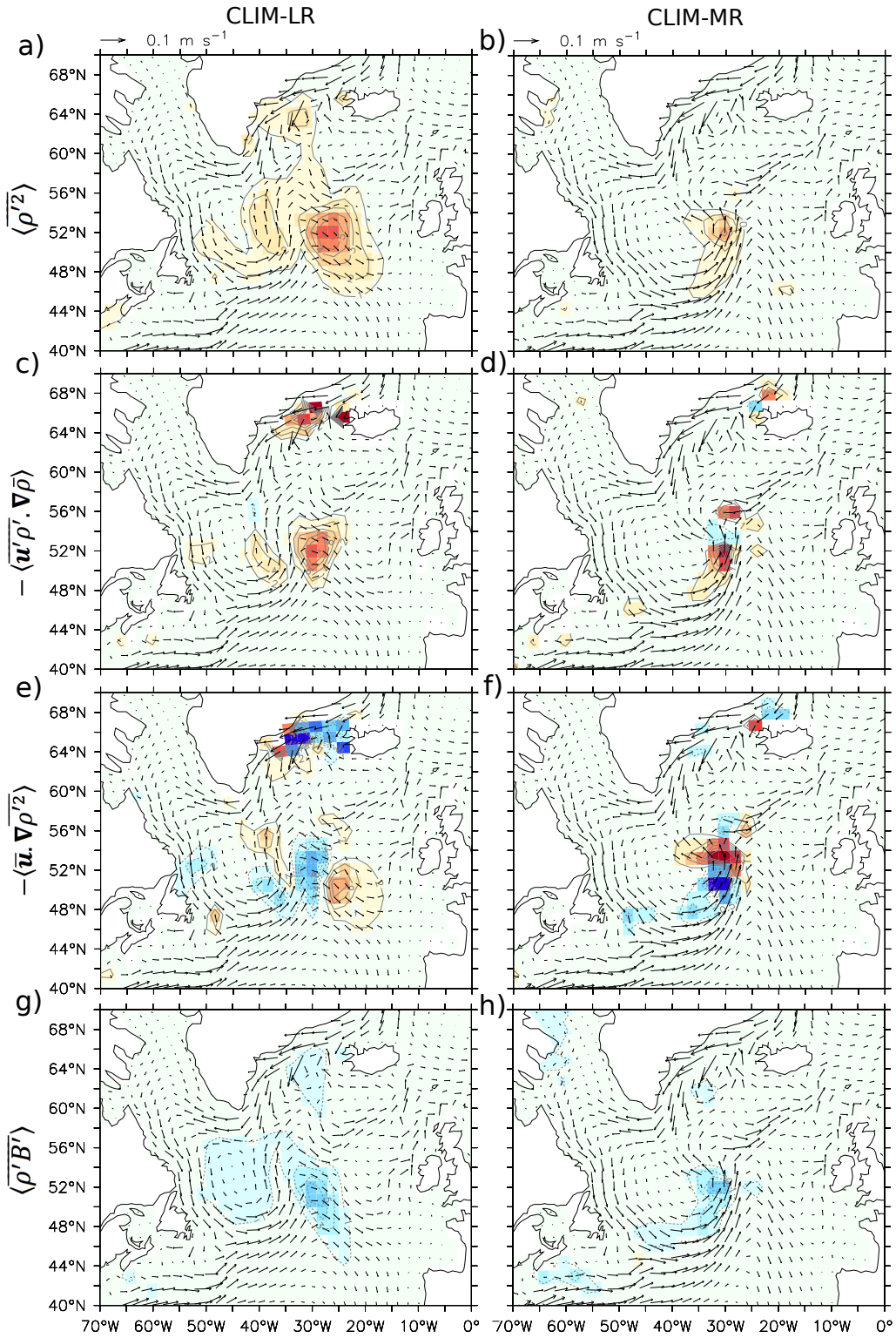

Figure 9:

Mean density interannual variance, at 0-700m depth (color shadings), in $(\text{kg m}^{-3})^2$, in (a) CLIM-LR and (b) CLIM-MR. Density variance tendency, in 10^{-3} $(\text{kg m}^{-3})^2$ yr^{-1}, induced by the eddy density transport down the zonal density gradient, in (c) CLIM-LR and (d)

CLIM-MR. (e) and (f) are the same as (c) and (d) but for the mean advection of density variance. Density variance tendency, in 10^{-4} (kg m^{-3})^2 yr^{-1}, induced by the surface buoyancy forcing, in (g) CLIM-LR and (h) CLIM-MR. In all panels, the vectors illustrate the mean oceanic current in the top 300 m. Note the difference in contour interval for CLIM-LR and CLIM-LR and in panels (a-f) and (g-h).

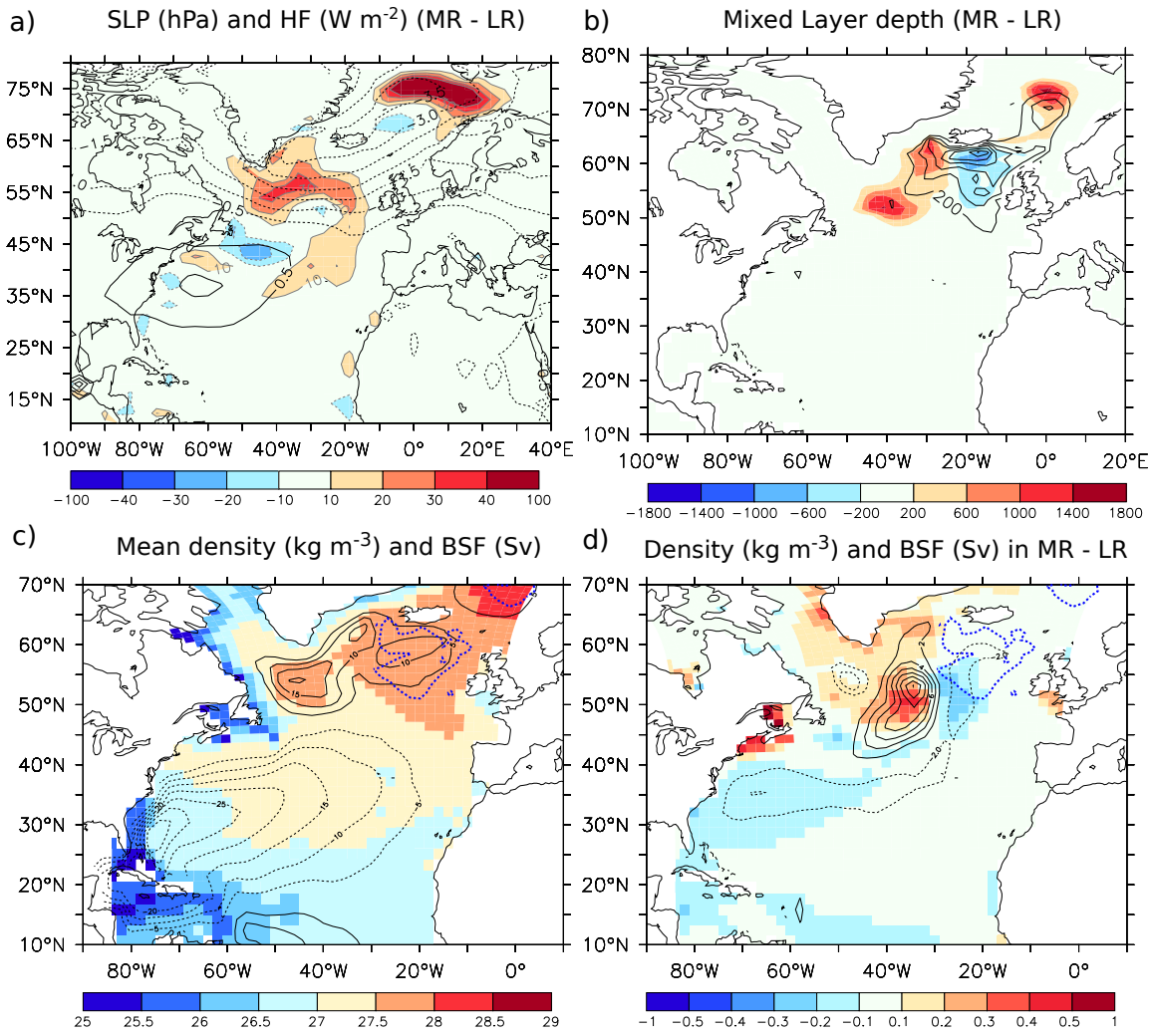

Figure 10:

(a) Mean surface heat flux (color, positive upward, in W m^{-2}), and (black contours) SLP, in hPa, difference between COUPLED-MR and COUPLED-LR simulation. (b) Mean FMA mixed layer depth difference (color, in m), between COUPLED-MR and COUPLED-LR simulation, and (black contours) mean FMA mixed layer depth in COUPLED-LR. (c) Mean subsurface potential density (color, in kg m^{-3}) for the upper 300m in CLIM-LR, and (black contours) mean barotropic streamfunction, in Sv. (d) Same as (c), but for the difference of the CLIM-MR and CLIM-LR. The thick blue dash contour in panels (c-d) indicates the difference in the yearly mixed layer depth standard deviation (contour interval 25m).

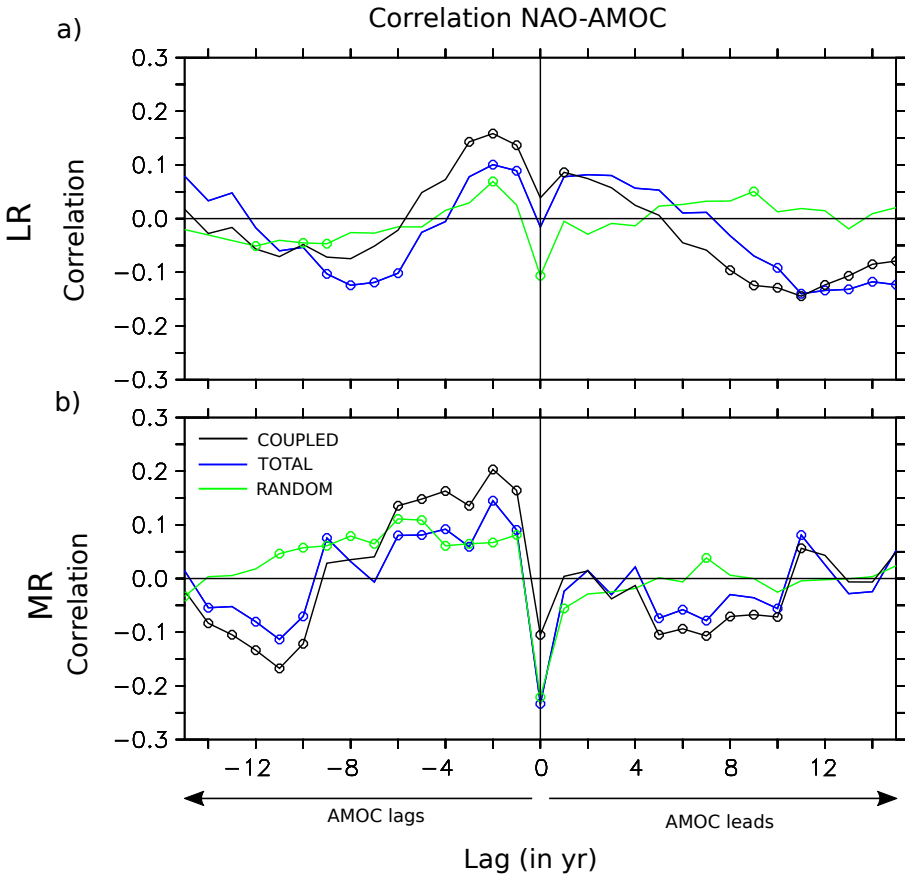

Figure 11:

Cross-correlation between the AMOC and the NAO indices in (a) LR and (b) MR simulations. The lag (in year) is positive when the AMOC leads. The color is black for the COUPLED simulation, blue for TOTAL, and green for RANDOM. The circles indicate level of significance below 5%.

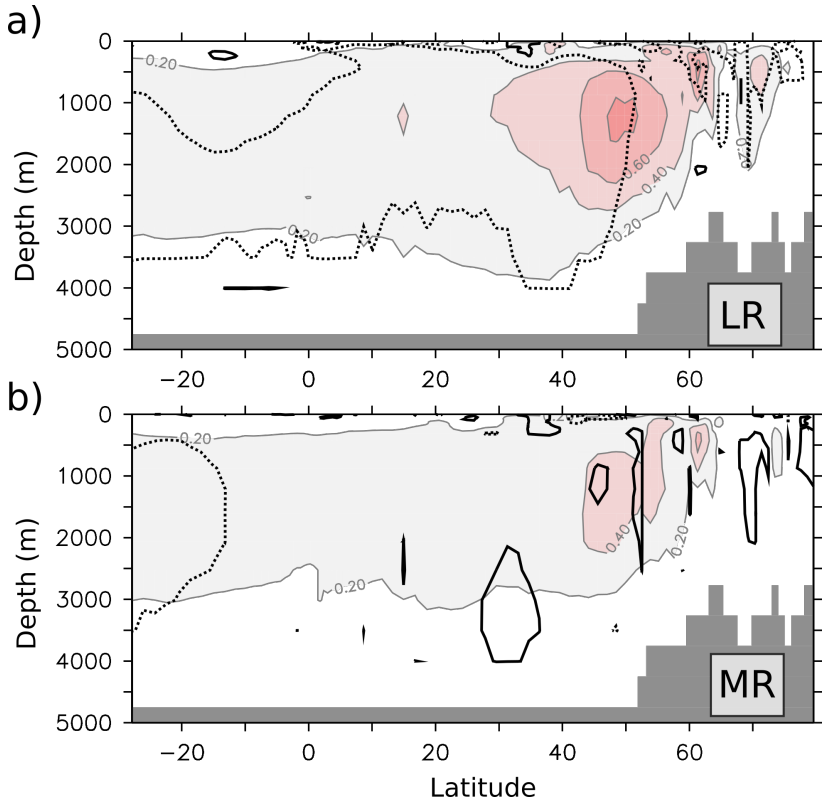

Figure 12:

(a) Standard deviation of the yearly band-pass (10-yr and 30-yr) filtered Atlantic meridional streamfunction, in Sv, for TOTAL-LR (shading). The thick black lines indicate where the variance for the yearly band-pass (10-yr and 30-yr) filtered streamfunction is lower (full line) or larger (dashed line) in RANDOM-LR when compared to TOTAL-LR, with a p-value lower than 5%. (b) Same as (a), but for the MR simulations.